Review of Scientific Instruments ARTICLE pubs.aip.org/aip/rsi

Calibration and characterization of the line-VISAR diagnostic at the HED-HIBEF instrument at the European XFEL

Cite as: Rev. Sci. Instrum. 96, 075206 (2025); doi: 10.1063/5.0271027
Submitted: 14 March 2025 • Accepted: 28 June 2025 •
Published Online: 22 July 2025

View Online Export Citation CrossMark

A. Descamps,[1,a)] T. M. Hutchinson,[2] R. Briggs,[2,3] E. E. McBride,[1] M. Millot,[2] T. Michelat,[4] J. H. Eggert,[2] B. Albertazzi,[5] L. Antonelli,[6,23] M. R. Armstrong,[2] C. Baehtz,[7] O. B. Ball,[8] S. Banerjee,[2,9] A. B. Belonoshko,[10,11] A. Benuzzi-Mounaix,[5] C. A. Bolme,[12] V. Bouffetier,[4] K. Buakor,[4] T. Butcher,[9] V. Cerantola,[13] J. Chantel,[14] A. L. Coleman,[2] J. Collier,[9] G. Collins,[15] A. J. Comley,[16] F. Coppari,[2] T. E. Cowan,[7] C. Crépisson,[17] G. Cristoforetti,[18] H. Cynn,[2] S. Di Dio Cafiso,[7] F. Dorchies,[19] M. J. Duff,[8] A. Dwivedi,[4] D. Errandonea,[20] E. Galtier,[21] H. Ginestet,[14] L. Gizzi,[18] A. Gleason,[21] S. Goede,[4] J. M. Gonzalez,[22] M. G. Gorman,[2,23] M. Harmand,[24] N. J. Hartley,[21] P. G. Heighway,[17] C. Hernandez-Gomez,[9] A. Higginbotham,[6] H. Höppner,[7] R. J. Husband,[25] H. Hwang,[25] J. Kim,[26] P. Koester,[18] Z. Konopkova,[4] D. Kraus,[7,27] A. Krygier,[2] L. Labate,[18] A. Laso Garcia,[7] A. E. Lazicki,[2] Y. Lee,[28] P. Mason,[9] M. Masruri,[7] B. Massani,[8] D. McGonegle,[16] C. McGuire,[2] J. D. McHardy,[8] R. S. McWilliams,[8] S. Merkel,[14] G. Morard,[29] B. Nagler,[21] M. Nakatsutsumi,[4] K. Nguyen-Cong,[22] A.-M. Norton,[6] I. I. Oleynik,[22] C. Otzen,[30] N. Ozaki,[31] S. Pandolfi,[32] D. J. Peake,[17] A. Pelka,[7] K. A. Pereira,[33] J. P. Phillips,[9] C. Prescher,[30] T. R. Preston,[4] L. Randolph,[4] D. Ranjan,[7] A. Ravasio,[5] R. Redmer,[27] J. Rips,[27] D. Santamaria-Perez,[20] D. J. Savage,[12] M. Schoelmerich,[34] J-P. Schwinkendorf,[7] S. Singh,[2] J. Smith,[9] R. F. Smith,[2] A. Sollier,[35,36] J. Spear,[9] C. Spindloe,[9] M. Stevenson,[27] C. Strohm,[25] T-A. Suer,[15] M. Tang,[25] T. Tschentscher,[4] M. Toncian,[7] T. Toncian,[7] S. J. Tracy,[37] M. Tyldesley,[9] C. E. Vennari,[2] T. Vinci,[5] T. J. Volz,[2] J. Vorberger,[7] J. P. S. Walsh,[33] J. S. Wark,[17] J. T. Willman,[22] L. Wollenweber,[4] U. Zastrau,[4] E. Brambrink,[4,b)] K. Appel,[4] and M. I. McMahon[8]

AFFILIATIONS

[1]School of Mathematics and Physics, Queen's University Belfast, University Road, Belfast BT7 1NN, United Kingdom
[2]Lawrence Livermore National Laboratory, Livermore, California 94550, USA
[3]Laser PI, Melbourne, Australia
[4]European XFEL, Holzkoppel 4, 22869 Schenefeld, Germany
[5]Ecole Polytechnique, Palaiseau, Laboratoire pour l'utilisation des Lasers Intenses (LULI), CNRS UMR 7605 Route de Saclay, 91128 PALAISEAU Cedex, France
[6]University of York, School of Physics, Engineering and Technology, Heslington York YO10 5DD, United Kingdom
[7]Helmholtz-Zentrum Dresden-Rossendorf (HZDR), Bautzner Landstraße 400, 01328 Dresden, Germany
[8]SUPA, School of Physics and Astronomy, and Centre for Science at Extreme Conditions, The University of Edinburgh, Edinburgh EH9 3FD, United Kingdom
[9]Central Laser Facility (CLF), STFC Rutherford Appleton Laboratory, Harwell Campus, Didcot OX11 0QX, United Kingdom
[10]Frontiers Science Center for Critical Earth Material Cycling, School of Earth Sciences and Engineering, Nanjing University, Nanjing 210023, China
[11]Condensed Matter Theory, Department of Physics, AlbaNova University Center, Royal Institute of Technology (KTH), 10691 Stockholm, Sweden

08 August 2025 08:10:42

© Author(s) 2025

[12]Los Alamos National Laboratory, Los Alamos, New Mexico 87545, USA
[13]Università degli Studi di Milano Bicocca, Dipartimento di Scienze dell'Ambiente e della Terra, Piazza della Scienza, 1e4 I-20126 Milano, Italy
[14]Univ. Lille, CNRS, INRAE, Centrale Lille, UMR 8207–UMET–Unité Matériaux et Transformations, F-59000 Lille, France
[15]University of Rochester, Laboratory for Laser Energetics (LLE), 250 East River Road, Rochester, New York 14623-1299, USA
[16]AWE, Aldermaston, Reading RG7 4PR, United Kingdom
[17]Department of Physics, Clarendon Laboratory, University of Oxford, Parks Road, Oxford OX1 3PU, United Kingdom
[18]CNR–Consiglio Nazionale delle Ricerche, Istituto Nazionale di Ottica, (CNR–INO), Via G. Moruzzi 1, 56124 Pisa, Italy
[19]Université de Bordeaux, CNRS, CEA, CELIA, UMR 5107, F-33400 Talence, France
[20]Universidad de Valencia–UV, Departamento de Fisica Aplicada–ICMUV, C/Dr. Moliner 50 Burjassot, E-46100 Valencia, Spain
[21]SLAC National Accelerator Laboratory, 2575 Sand Hill Road, Menlo Park, California 94025, USA
[22]Department of Physics, University of South Florida, Tampa, Florida 33620, USA
[23]First Light Fusion Ltd, Oxfordshire, United Kingdom
[24]PIMM, Arts et Metiers Institute of Technology, CNRS, Cnam, HESAM University, 151 Boulevard de l'Hopital, 75013 Paris, France
[25]Deutsches Elektronen-Synchrotron DESY, Notkestr. 85, 22607 Hamburg, Germany
[26]Hanyang University, Department of Physics, 17 Haengdang dong, Seongdong gu, Seoul 133-791, South Korea
[27]Universität Rostock, Institut für Physik, D-18051 Rostock, Germany
[28]Yonsei University, Department of Earth System Sciences, 50 Yonsei-ro Seodaemun-gu, Seoul 03722, Republic of Korea
[29]Univ. Grenoble Alpes, Univ. Savoie Mont Blanc, CNRS, IRD, Univ. Gustave Eiffel, ISTerre, 38000 Grenoble, France
[30]Institut für Geo- und Umweltnaturwissenschaften, Albert-Ludwigs-Universität Freiburg, Hermann-Herder-Straße 5, 79104 Freiburg, Germany
[31]Osaka University, Graduate School of Engineering Science, 2-1 Yamada-oka, Suita, Osaka 565-871, Japan
[32]Sorbonne Université, Muséum National d'Histoire Naturelle, UMR CNRS 7590, Insitut de Minéralogie, de Physique, des Matériaux, et de Cosmochinie, IMPMC, Paris 75005, France
[33]University of Massachusetts Amherst, Department of Chemistry, 690 N Pleasant St. Physical Sciences Building, Amherst, Massachusetts 01003-9303, USA
[34]Paul Scherrer Institut, Forschungsstrasse 111, 5232 Villigen, Switzerland
[35]CEA, DAM, DIF, 91297 Arpajon, France
[36]Université Paris-Saclay, CEA, Laboratoire Matière en Conditions Extrêmes, 91680 Bruyères-le-Châtel, France
[37]Carnegie Science, Earth and Planets Laboratory, 5241 Broad Branch Road NW, Washington, District of Columbia 20015, USA

[a)]**Author to whom correspondence should be addressed:** a.descamps@qub.ac.uk
[b)]**Electronic mail:** erik.brambrink@xfel.eu

ABSTRACT

In dynamic-compression experiments, the line-imaging Velocity Interferometer System for Any Reflector (VISAR) is a well-established diagnostic used to probe the velocity history, including wave profiles derived from dynamically compressed interfaces and wavefronts, depending on material optical properties. Knowledge of the velocity history allows for the determination of the pressure achieved during compression. Such a VISAR analysis is often based on Fourier transform techniques and assumes that the recorded interferograms are free from image distortions. In this paper, we describe the VISAR diagnostic installed at the HED-HIBEF instrument located at the European XFEL along with its calibration and characterization. It comprises a two-color (532, 1064 nm), three-arm (with three velocity sensitivities) line imaging system. We provide a procedure to correct VISAR images for geometric distortions and evaluate the performance of the system using Fourier analysis. We finally discuss the spatial and temporal calibrations of the diagnostic. As an example, we compare the pressure extracted from the VISAR analysis of shock-compressed polyimide and silicon.

© 2025 Author(s). All article content, except where otherwise noted, is licensed under a Creative Commons Attribution (CC BY) license (https://creativecommons.org/licenses/by/4.0/). https://doi.org/10.1063/5.0271027

08 August 2025 08:10:42

I. INTRODUCTION

Warm dense matter (WDM) is an exotic state of matter that occurs in fusion processes,[1–4] as well as in the interiors of giant planets and stellar accretion disks.[5–9] Accurately modeling WDM is challenging due to its position at the intersection of condensed matter physics and conventional plasma physics. Experimental studies are therefore essential for developing models that describe matter under extreme pressure and temperature conditions. A well-established method for generating WDM involves irradiating a solid-density target with a high-energy, nanosecond-long laser pulse.[10,11] The laser interacts with the target's front surface, creating an ablation plasma that expands outward from the target into the vacuum. By conservation of momentum, this process generates a compression wave traveling inside the target, in the opposite direction to the expanding plasma. The evolution of this compression wave is commonly diagnosed using a 1D line-imaging Velocity Interferometer System for Any Reflector (VISAR).[12–14] By measuring the phase shift of a laser reflected from a moving surface, VISAR provides a precise, high-temporal-resolution velocity profile as a function of position along a straight line on the target surface. This is achieved by projecting an image of the sample surface through an interferometer onto the entrance slit of a streak camera.[15,16] This technique enables precise characterization of the uniformity (planarity) of dynamic compression along the imaging direction. The reflecting surface can either be a free surface, a material interface within the compressed sample, or a reflecting shock front in an initially transparent material, yielding measurements of the free surface velocity, particle velocity, or shock velocity, respectively. In addition, VISAR can be used as an active shock breakout diagnostic to infer the average shock velocity through transit time measurements. We note that in this case, the accuracy of the inferred average velocity is often limited by the characterization of the sample thickness. Additionally, VISAR can be used as a diagnostic of sample optical properties, which may, in turn, be useful for temperature measurement and characterization of the sample state. When combined with mass, energy, and momentum conservation principles, these measurements provide insight into the time history of the longitudinal stress applied to the sample of interest.

With the recent commissioning of the high-repetition rate DiPOLE-100X long pulse laser system at the HED-HIBEF instrument,[17,18] we present the calibration and characterization of the 1D line-VISAR diagnostic for dynamic compression experiments. The raw VISAR images initially exhibit electron optics barrel-like distortions, which introduce a coupling between spatial and temporal dimensions. To address this, we implement a correction procedure based on non-linear mapping of control points between a distorted and a corrected Cartesian grid. The quality of the method is then evaluated by minimizing transverse wavevector components in the Fourier domain. Using the corrected images, we perform spatial and temporal calibration of the VISAR system installed at the HED-HIBEF instrument. Finally, we compare pressure measurements inferred from VISAR using polyimide and silicon samples shock-compressed using the DiPOLE-100X laser system.

II. DESCRIPTION OF THE VISAR SYSTEM

A VISAR system measures the Doppler shift of an optical probe as it is reflected from a moving target using interferometry, with typical implementations resulting in 10 m/s to 100 km/s velocity sensitivities.[14,19] It consists of a pulsed probe laser, an optical system that images a reflective surface on the rear side of the sample, an interferometer, and, for 1D line-VISAR, a streak camera. The probe laser pulse is back-reflected from a surface of the laser-compressed sample before passing through the interferometer and recorded on streak cameras.[20] The interferometer superposes in space two images of the reflecting surface with (1) an angle between their optical axes (producing fringes) and (2) a precise time delay, typically of order 1–1000 ps. When this interference pattern is recorded through the entrance slits of the streak cameras, the temporal evolution of the optical phase difference between the two images is captured along a straight line on the sample. The velocity profile of the moving interface can then be reconstructed with a few percent accuracy[15] from the differences in the resulting interferogram. The precise time delay between the two images is produced by inserting a flat and parallel AR-coated slab of UV-grade fused silica with precisely known thickness, known as an etalon, in one of the legs of the interferometer. The etalons used at the HED-HIBEF instrument are additionally treated with anti-reflection coatings for 532 and 1064 nm on both surfaces. Since the etalon displaces the image along the optical axis, the path length of the corresponding interferometer leg is compensated with μm-precision mechanized translation stages.[14] The etalon sets the velocity per fringe (VPF), which relates the measured phase shift to the velocity of the reflector. Further details on VISAR can be found in Refs. 14–16. Example VISAR images from shock-compressed samples at the HED-HIBEF instrument are shown in Sec. V.

A. General layout

The VISAR system at the HED-HiBEF instrument is designed as a versatile diagnostic for characterizing the sample evolution during laser-driven compression experiments. It consists of 3 VISAR arms—two operating at a wavelength of 532 nm and one at a wavelength of 1064 nm. In specific configurations, measuring reflectivity at two different wavelengths allows the extraction of material properties, such as AC conductivity.[21–23] Additionally, in cases where reflectivity or transparency at one wavelength is insufficient for measurement, the other wavelength may still provide useable data. The system also includes a line-imaging Streak Optical Pyrometer (SOP), which shares the same optical beam path, uses VISAR-inferred optical properties to establish the pyrometric temperature, and provides additional shock breakout information to complement the VISAR data in some experiments.[24–26]

The VISAR system is integrated into the HED-HiBEF experimental hutch, where two interaction chambers [IC1 for x-ray spectroscopy and IC2 for x-ray diffraction (XRD)] are installed to investigate laser-compressed matter using high-brilliance x rays provided by the European XFEL.[17] As a result, the VISAR system is designed to be compatible with experiments conducted in both chambers. To minimize interference with experiments that do not require VISAR, all components, including the streak cameras, interferometers, alignment cameras, and VISAR laser, are confined to a table, outside the interaction chambers, covering a total area of 1200×4000 mm^2 and a height of 2000 mm. All auxiliary supplies are located either on or below the table.

08 August 2025 08:10:42

© Author(s) 2025

Compared with VISAR systems found at other large facilities,[14,27–29] the VISAR system at the HED-HiBEF instrument is fully integrated into a control system with data acquisition up to 0.5 Hz. It includes four streak cameras: two ROSS 5800 Streak Camera Systems from Sydor Technologies for VISAR at a wavelength of 532 nm, one Hamamatsu C13410-02A used for VISAR at a wavelength of 1064 nm, and one Hamamatsu C13410-01A for Streaked Optical Pyrometry. The use of three VISAR arms is used to cover a wide range of detectable velocities. Additionally, the use of both 532 and 1064 nm probe wavelengths enables reflectivity measurements at two wavelengths. The ROSS 5800 cameras have two fiber-coupled inputs, allowing the injection of optical fiducials from both the drive laser pulse and the x-ray pulse. This setup helps accounting for the timing jitter caused by the electrical trigger distribution system in the data analysis, as discussed in Sec. IV A. The entrance slits of all streak cameras are oriented to spatially resolve the velocity profile along a horizontal line on the sample mounted in the interaction chamber.

An alignment camera (labeled Align. Camera. in Fig. 1) is installed on the second output of the interferometer. Its imaging lens is adjusted to provide a field of view (FoV) similar to that of the streak cameras. This camera serves multiple purposes. It is used to verify proper alignment of the beam transport and ensures correct overlap of images from both interferometer legs. Since the image position on the alignment camera varies with fringe orientation and spacing, it is used to set reference points for different fringe spacings. Finally, this camera is also used for the spatial calibration of the VISAR system, as described in Sec. IV A.

B. Beam transport and imaging system

The design of the beam path was guided by several key objectives: (1) minimizing chromatic aberrations in the transport optics at both 532 and 1064 nm wavelengths, (2) enabling measurements in both interaction chambers, (3) preventing vignetting for large FoV while using sufficiently large optics for efficient light collection, and (4) allowing FoV adjustments over a wide range with minimal setup modifications.

To achieve this goal, the entire system has been modeled using a ray-tracing code for different FoV settings, ensuring minimal vignetting, chromatic, and spherical aberrations.

As shown in Fig. 1, the system's core layout uses a single lens (L1) to transport the image of the sample in the IC2 target chamber center (TCC) to a first image plane (IP1) outside the interaction chamber. L1 is a F/2.3 (NA = 0.22), 168 mm focal length, custom-made triplet lens designed by OPA-OPTICAD to have an identical focal length for both 532 and 1064 nm, generating a 10× magnified image of the sample at IP1. The presence of a shield, made of fused silica or polycarbonate, to protect L1 from debris generated during the experiment was included in the design of L1. The subsequent beam transport experiences relatively low chromatic aberrations due to the system's high F-number, with any residual aberrations corrected in the final telescope before the streak camera. The image is relayed through a series of telescopes—L2/L3 within IC1 and L4/L5 leading to the VISAR table—where the beam is separated by wavelength. Each beam is then split between the different VISAR arms and finally directed to the streak cameras after passing through the interferometer. The interferometer is placed in a collimated section of the beam transport to reduce astigmatism and spherical aberrations, particularly when using long etalons, and the angle enclosed between the folded beams of the interferometer is ~15°. Despite the varying photocathode sizes of the streak cameras, an identical FoV is achieved across all streak cameras by

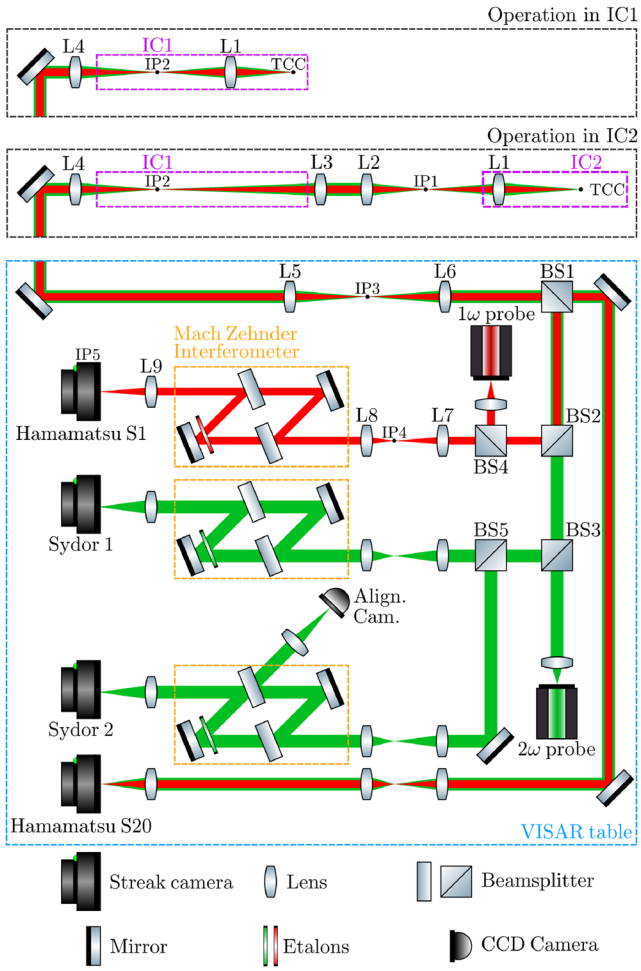


FIG. 1. Beam path of the VISAR system (not to scale). BS1 is a beam splitter reflecting 1064/532 wavelengths and transmitting broadband emission to the Hamamatsu S20. BS2 reflects 1064 nm and transmits 532 nm wavelengths. BS3, BS4, and BS5 are 50/50 beam splitters for 1064 and 532 nm, respectively. The VISAR probes at 532 and 1064 nm are injected through BS3 and BS4, respectively. The separation between the two probe wavelengths is performed using BS2. Depending on the interaction chamber used, the beam path is modified to follow either the black dashed rectangle "Operation in IC1" or "Operation in IC2." L3/L8 are 1520 mm focal length lenses from Edmund Optics (#50-107), L4/L5 are 850 mm focal length lenses from Edmund Optics (#30-976), L6 is a 500 mm focal length lens from Edmund Optics (#49-396), and L7 is a 750 mm focal length lens from Newport Corporation (#PAC097AR.14). For Sydor 1/2, L9 is an 850 mm focal length lens from Edmund Optics (#30-976). For Hamamatsu S1, in the VISAR mode, L9 is a 750 mm focal length lens from Newport Corporation (#PAC097AR.14). L9 is replaced by a 400 mm focal length lens from Edmund Optics (#88-598) in the SOP mode. For Hamamatsu S20, L8 is an 850 mm focal length lens from Edmund Optics (#30-976), and 9 is a 400 mm focal length lens from Edmund Optics (#88-598).

08 August 2025 08:10:42

© Author(s) 2025

adjusting the system magnification using the final telescope (L8-L9). In addition, a 532 ± 1 nm interference filter is inserted in front of the Sydor cameras to prevent the frequency-doubled DiPOLE-100X light from reaching the streak camera. For the Hamamatsu S1 camera, an RG1000 color filter and a 1064 ± 10 nm interference filter are used. The VISAR probe beam diameter is always smaller than 75 mm.

The mechanical setup supports etalons up to 200 mm in length, which defines the lowest velocity per fringe achievable: 0.248 and 0.514 km/s at 532 and 1064 nm wavelengths for fused silica etalons, respectively. A sensitivity of ~1/20 fringe can be achieved at the HED-HIBEF instrument. Table I lists the available etalons at the HED-HIBEF instrument. For etalon lengths up to 26 mm, it is possible to combine two etalons to fine-tune the VPF.

The FoV of the system can be modified by replacing lens L2. Since this lens is positioned near the imaged sample, changing it adjusts the FoV uniformly across all VISAR arms without affecting the fringe density on the streak cameras. Additionally, this modification scales the size of the probe laser beam on the sample. Information regarding the FoV and magnification for each lens L2 is shown in Table II.

Each image plane along the optical transport is equipped with removable fiducial markers (crosses, pinholes, and line grids) to facilitate quick alignment verification and diagnostic calibration. For example, a line grid in an image plane is used for spatial calibration of the streak cameras and correction of the streak camera distortions, as described in Sec. III. Crosses are used to align the interferometers. The image plane IP1 can also be utilized for sample alignment.

Additionally, the image plane within IC1 allows the laser to be used directly in this chamber. In this configuration, L1 is repositioned inside IC1, near the sample, to generate a primary image at the focal point of L4. Similar to L2, L4 is replaced to modify the diagnostic FoV during operations in IC1.

On the target side of L5, there is a possibility to inject light sources into the system to perform alignment tasks. White light can be used to equalize the length of the interferometer legs. A HeNe laser can be injected into the VISAR system or directed toward the sample, significantly simplifying optical alignment.

C. Performance

The spatial resolution of the VISAR system is primarily limited by the streak cameras, except for the largest FoV. Typically, the streak cameras resolve ~1:200 of the photocathode size. Since the FoV corresponds to the useable cathode size, the spatial resolution of the optical system can be approximated as FoV/200.

TABLE I. Available etalons with the corresponding VPF and temporal delay introduced between the two interferometer legs for each wavelength. The etalon thicknesses were measured within an uncertainty of 2 μm using a high-precision micrometer for etalons thinner than 25 mm. A micrometer with a 20 μm accuracy was used for the thicker ones. The expressions for the VPF and the etalon delay δ are taken from Barker and Schuler.[30] For the calculation, the refractive index (n_0) and dispersion correction ($dn/d\lambda$) for the UV-grade fused silica is taken to be (1.461, -46.31×10^{-3} μm^{-1}) at 532 nm and (1.450, -12.00×10^{-3} μm^{-1}) at 1064 nm using the data from Malitson.[31] We note that according to Celliers *et al.*,[14] the fast lens L1 introduces a ~1% correction to the VPF. This correction is larger than the thickness contribution to the uncertainty.

Length (mm)	VPF 532 nm (km/s)	Etalon delay τ 532 nm (ps)	VPF 1064 nm (km/s)	Etalon delay τ 1064 nm (ps)
3.171	15.64	16.48	32.42	16.14
4.954	10.01	25.75	20.75	25.21
7.182	6.905	37.34	14.31	36.55
11.15	4.446	57.98	9.217	56.77
17.18	2.887	89.29	5.985	87.41
26.16	1.896	136.0	3.930	133.1
69.95	0.7090	363.6	1.470	356.0
123.2	0.4027	640.2	0.8347	626.8
200.2	0.2477	1041	0.5136	1019

TABLE II. Field of View (FoV)/magnification for each diagnostic for different lens L2. The FoV is expressed in mm. F_{L2} denotes the focal length of lens L2. We note that for a given focal length of L2, the FoV and magnification are similar across all diagnostics.

F_{L2} (mm)	1520	850	400	200
Edmund optics part number	#50-107	#30-976	#88-598	#49-392
Sydor 1/2 (VISAR)	2.8/8x	1.6/14x	0.70/30x	0.35/60x
Hamamatsu S1 (VISAR)	2.5/7x	1.4/13x	0.66/27x	0.33/54x
Hamamatsu S20 (SOP)	2.5/7x	1.4/12x	0.66/27x	0.33/54x
Hamamatsu S1 (SOP)	2.3/8x	1.3/14x	0.60/29x	0.30/58x
Sydor 1/2 (SOP)	2.6/8x	1.4/15x	0.68/32x	0.34/64x

08 August 2025 08:10:42

© Author(s) 2025

The temporal resolution is determined by the sweep window length available on the streak cameras, as well as the streak camera entrance slit width. All streak cameras provide six sweep windows ranging from 1 to 100 ns (1, 5, 10, 20, 50, and 100 ns), with the 10, 20, 50 ns being the most common. Additionally, the Hamamatsu streak cameras offer extended sweep windows up to 1 ms, enabling longer-duration measurements. At the HED-HiBEF instrument, the streak camera entrance slit width is usually set to ~100 μm for the Hamamatsu streak cameras and ~500 μm for the Sydor streak cameras. Reducing the width of the slit would increase the temporal resolution at the expense of the intensity on the streak cameras.

The repetition rate of the system is constrained by the acquisition speed of the CCDs in the streak cameras. Currently, Sydor streak cameras are limited to 0.5 Hz although this restriction is partially due to network bandwidth, which can be improved. The Hamamatsu streak cameras can operate up to 10 Hz, the maximum repetition rate of the DiPOLE-100X laser system.

D. Probe laser

To ensure sufficient light collection from the sample reflection for the streak camera detectors, a pulsed fiber-coupled laser capable of supporting probe windows up to 100 ns, developed by the Laboratoire pour l'Utilisation des Lasers Intenses (LULI) in Palaiseau, France, and provided by the Helmholtz-Zentrum Dresden-Rossendorf (HZDR), Germany, is used. The maximum output energy is greater than 10 mJ, with the exact value depending on the duration of the pulse. To prevent damage to the optical fiber, the output energy is limited to ~2 mJ at 1064 nm and ~1 mJ at 532 nm. This laser delivers arbitrary pulse shapes. The pulse shaping capability is used either to match a square pulse to the acquisition window of the streak camera or to generate modulated picket pulses, used in the calibration, as described in Sec. III. For modulated picket pulses, the output energy is limited to 3 mJ, regardless of the pulse length, to limit pulse shape deformation due to the saturation of the laser amplifiers. In such cases, the pulse length is typically matched to the duration of the VISAR streak window. The approximately equal laser energy over the streak camera window results in similar counts on the CCD.

III. CORRECTION OF THE VISAR IMAGES

A. Procedure

The images recorded using the ROSS 5800 cameras are particularly susceptible to geometrical distortions caused by static distortions—from the streak tube, the imaging system, and barrel distortions in the electron optics—and sweep speed non-linearity—a non-linear relationship between the pixel position and absolute time on the streak camera. Additionally, these streak cameras use a curved phosphor screen that matches the focal plane curvature, resulting in improved image quality and temporal resolution toward the edges of the active image area. This improvement comes at the expense of strong distortions that create a coupling between the horizontal (time) and vertical (space) axes, thus hindering image analysis. These distortions can be seen in the raw image at the top of Fig. 2 and need to be corrected.

This paper describes a post-processing approach developed in support of the first community-proposal experiment (p2740) using

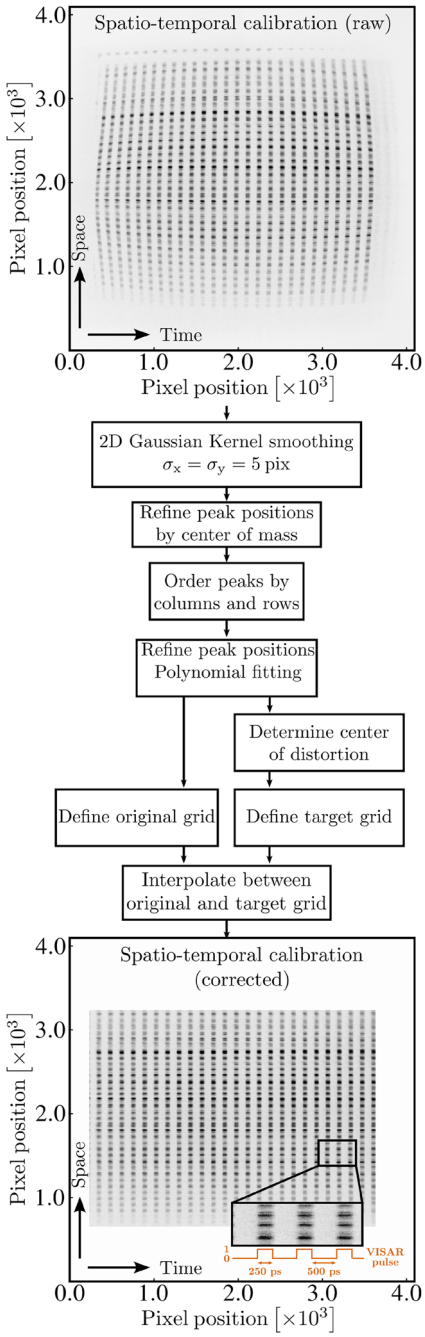


FIG. 2. Procedure to correct for the distortion of the VISAR images. The image at the top corresponds to the spatiotemporal calibration using a 20 ns VISAR sweep window. The modulation along the horizontal direction is generated by modulating the output of the VISAR laser such that the laser is ON for 250 ps and OFF for 500 ps, as shown in the bottom figure. In the vertical direction, the modulation corresponds to the interference pattern generated by the VISAR interferometer. After identifying each dark spot, the original (warped) and target (dewarped) grids are defined. The corrected image on the right is finally obtained after a double interpolation on the pixel position and intensity using the original and target grids. Each step is detailed in the Jupyter notebooks available online (see the data availability statement).

08 August 2025 08:10:42

© Author(s) 2025

the DiPOLE-100X laser system at the HED-HIBEF instrument at the European XFEL. Notably, the distortions on the Hamamatsu cameras are, by design, not as large as those of the ROSS 5800, meaning they do not require this correction, although the sweep non-linearity still needs compensation for accurate time reconstruction.

To correct the geometrical distortions, a spatiotemporal calibration image is recorded on the streak cameras.[32] This calibration image consists of a grid of control points that enables mapping between the original (distorted) and corrected images, where the axes are properly decoupled. The horizontal (time) spacing on the image is obtained by modulating the temporal profile of the VISAR laser using an arbitrary wavefront generator with a minimum time increment of 100 ps. The use of the pulse-shaping capabilities of the VISAR probe laser in the generation of the spatiotemporal calibration sets apart the system at the HED-HiBEF from designs found at other large-scale laser facilities. The vertical modulation is introduced either by the interferometer or by a vertical line grid positioned in the intermediate image plane (IP3) of the VISAR optical path.

An example of such a calibration image is shown at the top of Fig. 2, where the vertical modulation was generated by the interferometer and the temporal modulation is achieved by turning the VISAR output ON for 250 ps and OFF for 500 ps, as shown at bottom of Fig. 2. The procedure used is summarized in Fig. 2. The first step involves identifying the centroid of the regions corresponding to the signal when the laser is ON. To achieve this, we first apply a 2D Gaussian convolution kernel with a standard deviation of 5 pixels to the full image to smooth the intensity within each control region to better identify their position. The peaks are then identified on the basis of their signal level and distance from each other. In principle, the intensity within each control region should be uniform as the VISAR is either ON or OFF. In practice, a binary image, with a threshold of 80% of the maximum value, is constructed for each smoothed control region. This threshold value was found to be sufficient to prevent interference from neighboring control regions. The control point position is then refined by calculating the center-of-mass of the binary image. This step ensures that the refined positions do not fluctuate within each control region. The refined positions belonging to the same "curved column" are fitted with a 1D polynomial, as shown in Fig. 3. The same procedure is repeated for the refined positions belonging to the same "curved row." The final control points are obtained from the intersection of each fitted "curved row" with each "curved column." We found that a sixth order polynomial was required to accurately reproduce the distortion of the image close to the edges of the streak camera, as shown in Fig. 3(c). Even though the distortion is less severe for the "curved rows," the same polynomial order is applied for all "curved rows" and "curved columns."

Since the vertical and horizontal axes in the corrected grid should be decoupled, the distorted grid should map onto a Cartesian grid with fixed horizontal (time) and vertical (space) increments. These increments correspond to the spacing between the control points closest to the center of distortion of the image. In this region, geometrical distortions are minimal, and the control points follow a Cartesian grid. The center of distortion is obtained from the intersection of the row and column, which minimizes the maximum distance between their control points. Once the center of distortion and increments are known, the Cartesian grid is defined across the

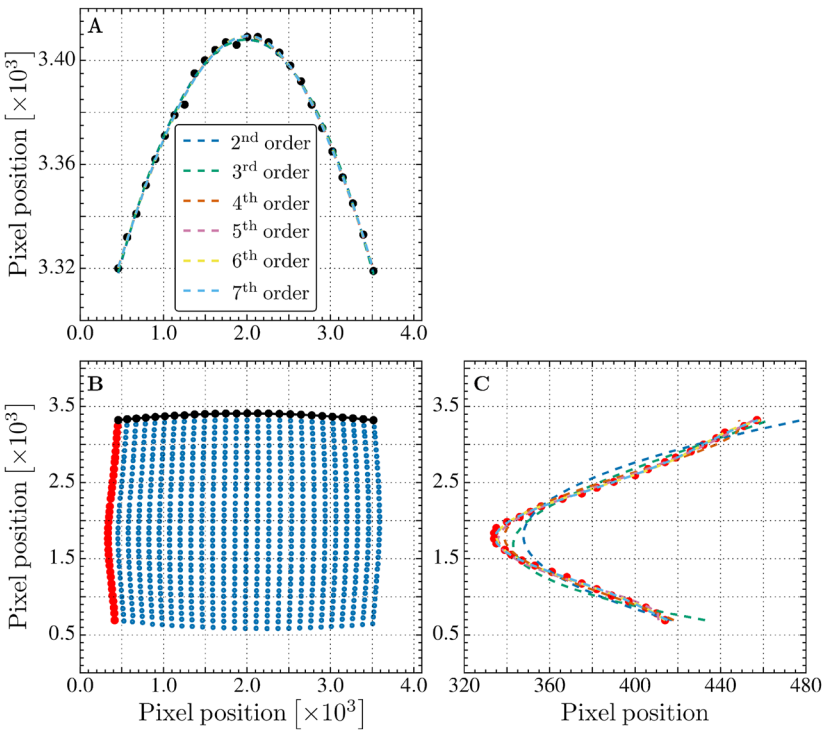


FIG. 3. Refinement of the control point positions using 1D polynomial fitting. (b) The blue circles corresponds to the control points obtained from the spatiotemporal calibration shown in Fig. 2. These control points are ordered in "curved rows" and "curved columns." Black (red) symbols show an example of a "curved row" ("curved column"). (c) Results of the 1D polynomial fitting of the left-most "curved column" [red data points in (b)]. The corresponding root mean square residuals are 59, 43, 22, 11, 6.6, and 5.5 for increasing polynomial order. (a) Results of the 1D polynomial fitting for the top-most "curved row."

08 August 2025 08:10:42

© Author(s) 2025

entire spatiotemporal calibration image. Upon inspection of Fig. 4, we observe that the corrections between the control points on the raw image (x_r, y_r) and the corresponding points on the Cartesian grid (x_c, y_c) in both the horizontal and vertical directions are more complex than a simple barrel distortion as they do not only depend on the Euclidian distance between (x_r, y_r) and the center of distortion. As a result, two bicubic interpolation functions are created to map the pixel position and intensity of each pixel from the control points on the original grid to control points on the corrected Cartesian grid. By construction of the Cartesian grid, both geometric distortions and sweep speed non-linearity are corrected in the final image. We note that only the region covered by the control points in the original images and, hence, within the validity domain of the interpolation functions is corrected. As a result, even though the CCD is 4096 × 4096 pixels, only an area of 3500 × 2300 pixels can be corrected. It is worth mentioning that thin-plate splines (TPSs) have been used in previous work to map the control points on the original grid to control points on the corrected Cartesian grid.[33] We compared the corrected images using both interpolation functions and found little difference with the bicubic interpolations described in this paper.

The procedure described above is repeated at the beginning of each experimental campaign, with a campaign spanning up to 6 days. In practice, we found a 25 ps root mean square error on the temporal axis when correcting a spatiotemporal image collected in November 2024 using a calibration from March 2023.

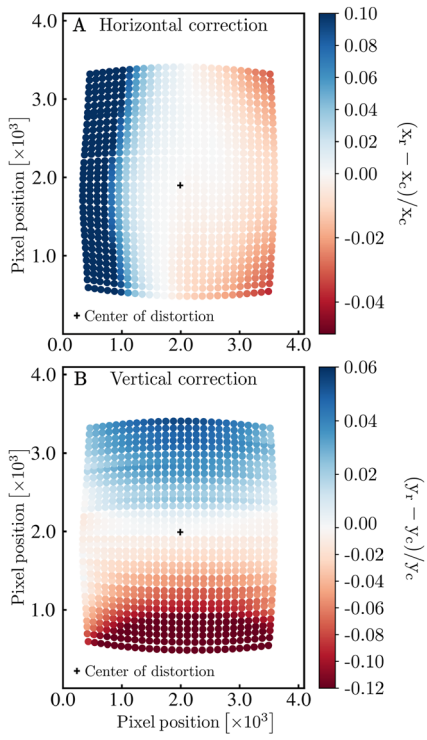


FIG. 4. (a) Horizontal and (b) vertical correction map between the control points on the raw image and the corrected image. The correction is evaluated by $(x_r - x_c)/x_c$ and $(y_r - y_c)/y_c$ for the horizontal and vertical directions, respectively. (x_r, y_r) defines the coordinate of the control points in the raw spatiotemporal calibration image obtained following the procedure shown in Fig. 2. (x_c, y_c) defines the corresponding coordinates of on the corrected image. The center of distortion is shown with the black crosses.

B. Evaluation

To assess the performance of the procedure described in Sec. III A, we compare the two-dimensional Fast Fourier Transform (2D-FFT) of both raw and corrected VISAR images. For this, images of a stationary, highly reflective reference sample are measured on both arms of the VISAR system using a flat-top VISAR probe laser pulse longer than the sweep window. In contrast to the previous section, for a stationary target, we expect that the fringe pattern remains unchanged during the duration of the streak camera sweep, resulting in "horizontal" fringes in the streaked images. As expected, distortions are clearly visible in Fig. 5(c). While we focus on VISAR 2 with a 20 ns VISAR sweep window, the same conclusions apply to VISAR 1 and other sweep windows. Before applying the 2D-FFT, images are cropped to 2500 × 1600 pixels to remove parasitic frequency components from the boxcar function associated with the limited corrected area. The results of the 2D-FFT are shown in Figs. 5(a) and 5(b). Upon inspection of the FFTs, the intensity around $k_x \sim 0$ pix^{-1} is wider for the raw image compared to the corrected image. Additionally, one observes horizontal streaks at the carrier frequency in (a), indicating the presence of transverse wavevectors with horizontal components, leading to fringe curvature. In contrast, the power spectrum of the corrected images is mostly concentrated along $k_x \sim 0$ pix^{-1}, indicating reduced distortion. To further highlight the reduction, we show the raw and corrected images after removing the $k_x \sim 0$ pix^{-1} component in the interferograms (a) and (b). This procedure effectively removes the components of the images with perfectly horizontal fringes such that only the distortions are left in (c) and (d). We observe that image (d) does not present visible curvature when compared to (c).

Although the distortion of the VISAR images was found to be independent from the VISAR sweep window duration, the calibration procedure corrects for the non-linearity of the streak camera, which depends on the VISAR sweep window. As a result, the calibration procedure should be performed for each VISAR sweep window.

IV. CALIBRATION OF THE VISAR DIAGNOSTIC

A. Time calibration of the VISARs

Using the procedure described in Sec. III, the mapping between the pixel position (horizontal axis) and absolute time is, by construction, linear for both VISAR 1 and VISAR 2. To verify this and obtain a precise time calibration, we measure the temporal profile of a 10 ns laser pulse generated by DiPOLE-100X directly on the streak cameras. The calibration is carried out by directing a low-energy laser pulse onto a frosted plastic sample placed at the target position. The scattered light is collected by the in-vacuum VISAR lens (L1) and relayed to the streak cameras after blocking one arm of the interferometer and removing the interference filters. The temporal profile of the DiPOLE-100X laser pulse is shown in Figs. 6(a) and 6(b) (black dashed rectangles). The time calibration is then determined by varying the arrival time of the laser pulse on the streak

08 August 2025 08:10:42

© Author(s) 2025

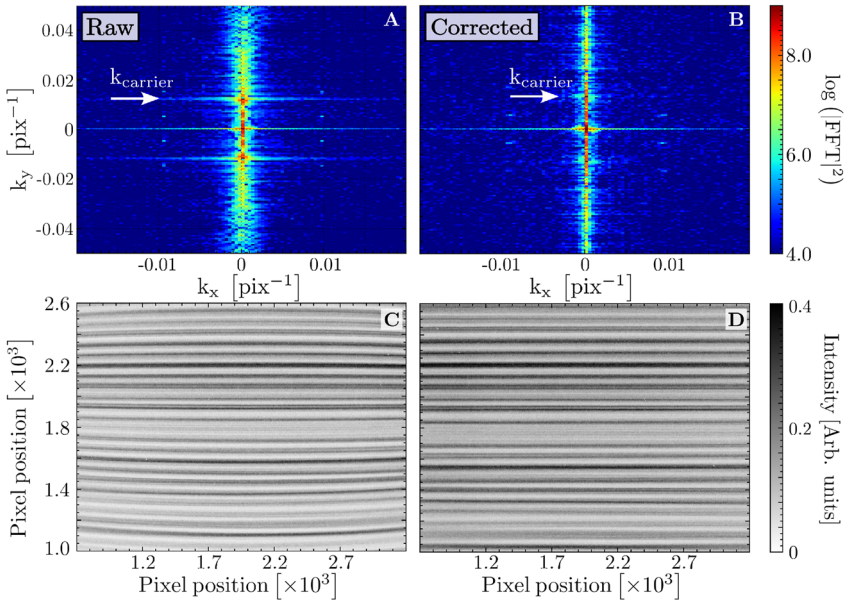


FIG. 5. Log-power spectrum of the 2D Fast Fourier Transform (FFT) of the raw (a) and corrected VISAR 2 image (b). The log-power spectra are zoomed in to highlight the frequency components around the carrier frequency $k_{carrier}$ of the interferograms indicated by the white arrows. The images filtered for the $k_x = 0$ pix^{-1} component is shown in (c) for the raw and (d) for the corrected image. The VISAR images were collected using a 20 ns sweep window and a static sample.

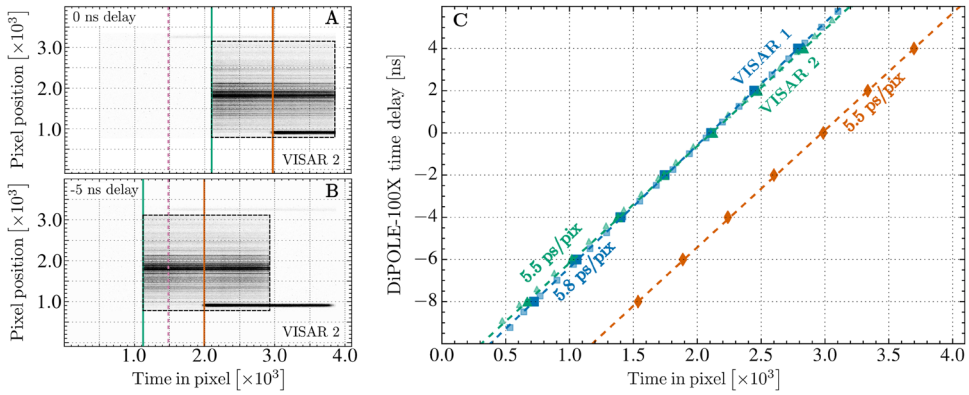


FIG. 6. Corrected images for the second arm of the VISAR system for a DiPOLE-100X time delay of 0 ns (a) and −5 ns (b). The black dashed rectangles across the streak window highlight the position of a 10 ns square pulse on the streak camera for different time delays. The narrow dark signal at the bottom of the image corresponds to the DiPOLE-100X fiducial. The rising edges of the DiPOLE-100X and fiducial are shown by the green and orange vertical lines, respectively. The pink dashed line corresponds to the position of the x-ray fiducial shown by the faint signal at the top of the image. The positions of the rising edges of both fiducials are recorded for several time delays of DiPOLE-100X, and the results are shown in figure (c) with the corresponding colored symbols. The blue symbols in (c) correspond to the positions of rising edges of the DiPOLE-100X laser profile on VISAR 1, not shown for clarity in (a) and (b). Here, the positions of the rising edges are defined as the mid-height point and are obtained by fitting an error function to the rising edge. The smaller faint symbols for VISAR 1 and VISAR 2 correspond to the temporal calibration obtained using the corrected spatiotemporal image shown at the bottom of Fig. 2.

cameras and monitoring the position of the rising edge of DiPOLE-100X and its fiducial. Figures 6(a) and 6(b) show the measurement with a DiPOLE-100X time delay of 0 ns and −5 ns.

To establish the pixel-to-time conversion, we fit the position of the rising edges for several DiPOLE-100X delays, shown in Fig. 6(c), using a third-order polynomial $\left(T(p) = A_1 \times p + A_2 \times p^2 + A_3 \times p^3\right)$. The coefficients of the polynomial used to convert the pixel coordinates (p) of the full images to time coordinates are summarized in Table III. For VISAR 1 and VISAR 2 (Sydor cameras), only A_1 is non-zero, as expected for a linear relationship between the pixel position and time. However, for VISAR 3 (Hamamatsu camera), higher-order terms (A_2, A_3) are present, which account for sweep non-linearity in that system. These additional terms are obtained using a spatial-temporal calibration image recorded on VISAR 3. The absolute time axis is then computed using the following equation:

$$t = T(p) - T(p_0) + D - S, \tag{1}$$

08 August 2025 08:10:42

© Author(s) 2025

TABLE III. Polynomial coefficients corresponding to the temporal calibration of each VISAR arm for the 10, 20, and 50 ns sweep windows. Here, p corresponds to the pixel coordinate along the horizontal axis. It spans [0, 4096] for the Sydor cameras and [0, 1344] for the Hamamatsu camera. The time calibration for each VISAR is obtained from Fig. 6.

		Polynomial $\left[A_1 \times p + A_2 \times p^2 + A_3 \times p^3\right]$		
Diagnostic	Sweep window (ns)	A_1(ns/pix)	A_2(ns/pix^2)	A_3(ns/pix^3)
Sydor 1(VISAR 1)	10	$2.81(3) \times 10^{-3}$	0	0
	20	$5.80(5) \times 10^{-3}$	0	0
	50	$14.5(6) \times 10^{-3}$	0	0
Sydor 2(VISAR 2)	10	$2.67(0) \times 10^{-3}$	0	0
	20	$5.53(8) \times 10^{-3}$	0	0
	50	$14.3(9) \times 10^{-3}$	0	0
Hamamatsu S1(VISAR 3)	10	$8.06(4) \times 10^{-3}$	$-1.02(7) \times 10^{-6}$	$3.32(2) \times 10^{-10}$
	20	$1.42(9) \times 10^{-2}$	$-5.21(3) \times 10^{-8}$	$3.37(8) \times 10^{-10}$
	50	$3.94(4) \times 10^{-2}$	$-2.01(2) \times 10^{-6}$	$8.88(6) \times 10^{-10}$

with t being the absolute time axis corresponding to pixel p. p_0 is the pixel corresponding to the position of the rising edge of the DiPOLE-100X laser pulse for a delay of 0 ns, as shown in Fig. 6(c). Term D represents the DiPOLE-100X time delay, while S is the sweep window delay of the streak camera. Adjusting S by a positive value can be useful in cases where the time required for the compression wave to reach the interface of interest exceeds the sweep window duration. In this case, the dashed black rectangles in Figs. 6(a) and 6(b) shift to earlier times (toward the left), hence the negative sign in Eq. (1). We note that the value of p_0 should be determined for each experimental campaign. Given the full size of the VISAR 1 and VISAR 2 images, it may be beneficial to downsample them for memory efficiency and signal to noise ratio improvements. If downsampling by a factor k, coefficient A_1 needs to be adjusted to $k \times A_1$.

Using the calibrations for the two Sydor cameras, a 10 ns square pulse generated by DiPOLE-100X exhibits a rise time from 10% to 90% of its final value in 200 ± 50 ps for VISAR 1 and 200 ± 80 ps for VISAR 2, measured using a 20 ns sweep window. These measurements were obtained using a 20 ns VISAR sweep window for each arm, with uncertainties reported at the 1σ level. Additionally, a leakage of the DiPOLE-100X pulse is recorded and serves as a timing fiducial, visible at the bottom of the VISAR 2 image in Figs. 6(a) and 6(b). The rising edge of this fiducial [orange diamond data in Fig. 6(c)] provides a precise reference for determining the laser pulse arrival time during shock compression experiments. Notably, the time calibrations derived from both the DiPOLE-100X pulse profile and the fiducial are identical, confirming that the time axis is consistent across the spatial dimension and only requires a simple linear time calibration.

The temporal axis is thus established relative to the arrival time of the DiPOLE-100X laser pulse at the sample position. However, because the laser system is synchronized with the x-ray beam delivered by the European XFEL, it is essential to measure the arrival time of the x-ray pulse on each arm of the VISAR system. This measurement is achieved by detecting the x-ray induced reflectivity loss of a thin foil using the streak cameras. However, depending on the target assembly, this signal may not always be available. In such cases, an x-ray timing fiducial is utilized. This fiducial is generated using the fluorescence signal from a 50 μm-thick YAG window located in IC1, several meters upstream of the sample position to ensure minimum contribution to the shock measurements performed in IC2. Since the presence of the YAG window still attenuates the x-ray beam, it is often removed once the x-ray timing is confirmed to maximize the photon flux reaching IC2. The fluorescence signal is transmitted to the VISAR 2 streak camera through an optical fiber. Although weaker than the DiPOLE-100X fiducial, the x-ray fiducial is still visible at the top of VISAR 2, as indicated by the pink vertical dashed line in Figs. 6(a) and 6(b).

To quantify the uncertainties in the time calibration, we analyze the contributions from both the long-pulse laser and the streak cameras by examining the correlation between the rising edge positions of the DiPOLE-100X laser pulse, the DiPOLE-100X fiducial, and the x-ray fiducial.

1. The difference between the relative timing of the DiPOLE-100X pulse on VISAR 2 and the DiPOLE-100X fiducial is examined, as shown with the blue dataset in Fig. 7. Since both signals are recorded on the same streak camera, the timing difference represents the intrinsic time resolution of the streak camera, which is found to have a standard deviation of 13 ps for both VISAR arms and for a 20 ns sweep window.
2. The difference between the DiPOLE-100X timing on VISAR 2 and DiPOLE-100X timing on VISAR 1 (orange data in Fig. 7) provides information about the timing jitter between the two arms of the VISAR system. Because both rising edges originate from the same laser pulse, any shift in arrival time affects both measurements identically. The measured timing jitter between the two arms is found to be 24 ps.
3. Finally, the difference between the rising edge position of the x-ray fiducial and DiPOLE-100X fiducial—both measured on the same streak camera—gives access to the timing jitter of the

08 August 2025 08:10:42

© Author(s) 2025

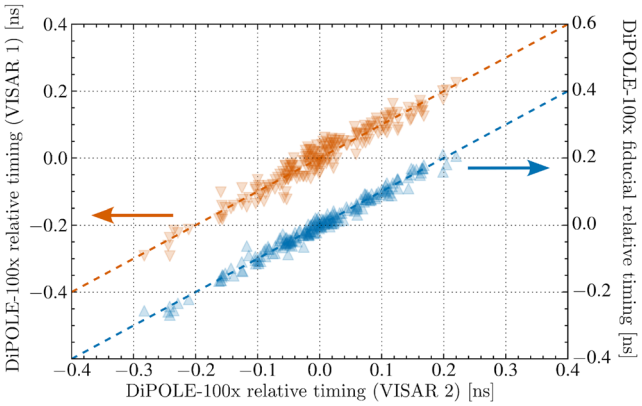


FIG. 7. (Orange inverted triangles) Correlation between the timing of DiPOLE-100X on VISAR 2 and VISAR 1. (Blue triangles) Correlation between the timing of DiPOLE-100X on VISAR 2 and DiPOLE-100X fiducial. The datasets are offset vertically for clarity. The dashed lines correspond to a unity slope line and are found to be a good approximation for the first principal component of each dataset.

DiPOLE-100X laser pulse relative to the x-ray beam. This jitter is measured to be ~90 ps, as shown in Fig. 8.

From the relative timing of DiPOLE-100X, Fig. 7, we find that the jitter in the arrival time of the DiPOLE-100X laser pulse is 94 ps for VISAR 1 and 92 ps for VISAR 2. These values correspond to the standard deviation of the blue and orange datasets. However, most of this jitter can be corrected by referencing the DiPOLE-100X fiducial to determine the precise arrival time of the DiPOLE-100X laser pulse, ultimately resulting in a probing time jitter of ~90 ps between the x-ray pulse and the DiPOLE-100X laser pulse. It is worth mentioning that the timing uncertainties between the two VISAR arms are correlated. This correlation is evident in Fig. 7, where the orange data points remain linearly correlated, despite being recorded on different streak cameras. In conclusion, by using the fiducials recorded on VISAR 2, a timing error of at most ~90 ps between the x-ray beam and the DiPOLE-100X laser pulse can be achieved.

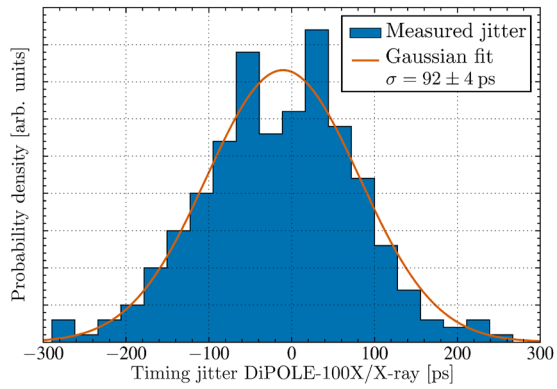


FIG. 8. Distribution of the timing difference between DiPOLE-100X and the x-ray beam measured using their respective fiducial on VISAR 2 (blue histogram). The orange curve shows the normal distribution with a standard deviation σ = 92 ± 4 ps, best explaining the measurements within a Bayesian framework. This parameter corresponds to the mean posterior estimate obtained using Markov Chain Monte Carlo performed with the PyMC package.

B. Spatial calibration of the VISARs

The spatial calibration of the VISAR system follows a two-step procedure. As described in Sec. II, the system is designed to accommodate different FoVs by changing lens L2. The first step involves cross-calibrating the pixel axis between the streak cameras and the VISAR alignment camera (labeled Align. Cam. in Fig. 1 and referred to as *HED_EXP_VISAR/CAM/ARM_2_INTERF* in the data acquisition system at the HED HIBEF instrument). This is achieved using a calibration sample positioned at IP3. In the second step, another calibration sample is placed at TCC to form an image on the VISAR alignment camera. This method isolates a section of the optical beam path that remains unaffected by the choice of L2, simplifying the overall alignment process. Since L2 is the only adjustable element, the magnification between IP3 and the streak cameras needs to be determined only once.

The first step of this calibration procedure is illustrated in Fig. 9, which demonstrates the cross-calibration between the spatial axis of VISAR 2 and the spatial axis of the VISAR alignment camera. A bar grid calibration sample is placed at IP3 and simultaneously imaged

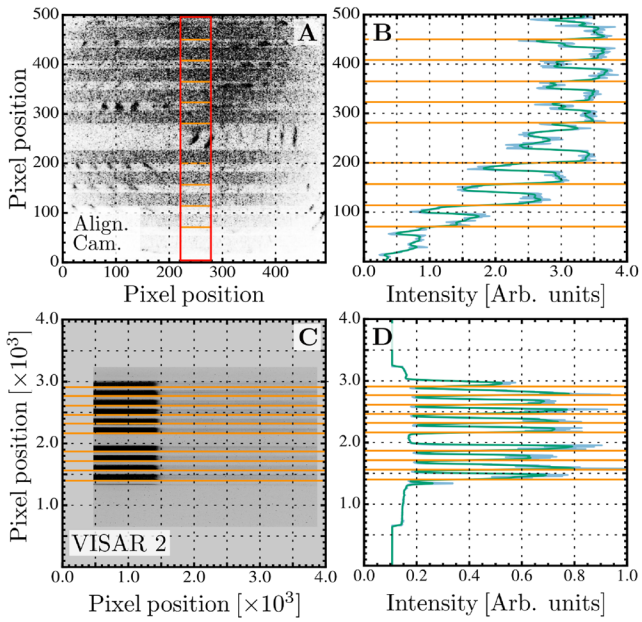


FIG. 9. Cross-calibration procedure between the VISAR alignment camera and the streak camera of VISAR 2. A bar grid is imaged on the VISAR alignment camera (a). (b) Corresponding raw vertical lineout signal (blue) and smoothed vertical lineout (green). The position of the rising edges of each bar is defined as the maxima of the smoothed signal derivative and is highlighted with the orange horizontal lines. The smoothed lineout was obtained by convolving the raw intensity using a Gaussian kernel with a standard deviation of 20 pixels. The red box in (a) corresponds to the spatial dimension of the entrance slit of the streak camera. We note that the alignment camera image has been rotated 90°. In practice, the slits at the entrance of the streak cameras are all horizontal. The same bar grid is simultaneously measured on the streak camera of VISAR 2 (c), and the same analysis is used to identify the bar positions (d).

08 August 2025 08:10:42

© Author(s) 2025

TABLE IV. Cross-calibration between the VISAR alignment camera and the three VISAR legs used at the HED-HIBEF instrument. These values are independent of lens L2 defining the FoV. The values for the spatial calibration of all VISARs are calculated for different FoVs. The results are obtained following the procedure presented in Fig. 9.

Diagnostic	Cross-calibration with align. cam	Spatial calibration F_{L2} = 400 mm FoV ≈ 0.4 mm	Spatial calibration F_{L2} = 850 mm FoV ≈ 0.8 mm	Spatial calibration F_{L2} = 1520 mm FoV ≈ 1.8 mm
Sydor 1 (VISAR 1)	×3.7 ± 0.1	0.21 ± 0.01 μm/pix	0.58 ± 0.02 μm/pix	0.80 ± 0.03 μm/pix
Sydor 2 (VISAR 2)	×3.5 ± 0.1	0.22 ± 0.01 μm/pix	0.61 ± 0.02 μm/pix	0.84 ± 0.04 μm/pix
Hamamatsu S1 (VISAR 3)	×1.4 ± 0.1	0.55 ± 0.01 μm/pix	1.52 ± 0.06 μm/pix	2.10 ± 0.10 μm/pix

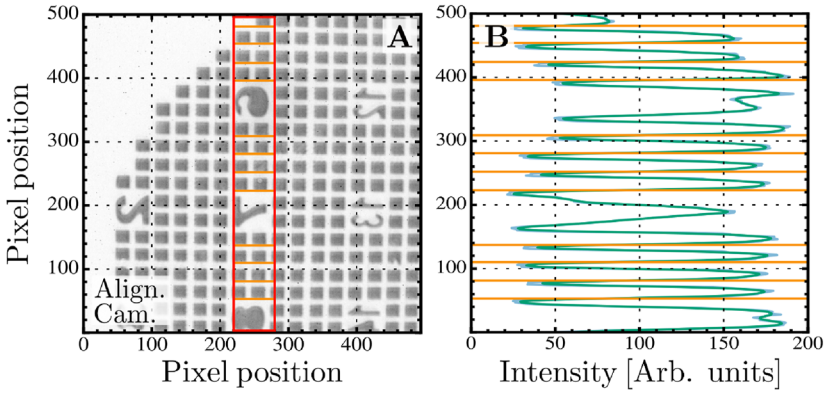


FIG. 10. Spatial calibration procedure. A copper TEM grid positioned at TCC is imaged onto the VISAR alignment camera (a). (b) The corresponding raw vertical lineout signal (blue) and smoothed vertical lineout (green).

on both the VISAR alignment camera (a) and VISAR 2 (c). A vertical lineout is taken to measure the spacing between the bars on each camera, as depicted in panels (b) and (d). For the case shown in Fig. 9, the bar spacing on VISAR 2 is found to be 3.5(1)× larger than that measured on the VISAR alignment camera. This same analysis is applied to the other VISAR arms, and the results are summarized in Table IV.

The second step of the calibration procedure uses a grid pattern, shown in Fig. 10(a), inserted at TCC and imaged onto the VISAR alignment camera. The grid consists of a copper TEM grid from Science Services (Ref. G400F1-Cu), with bar sizes of 15 μm and a hole spacing of 47 μm. Using a vertical lineout, we find that the horizontal bars are separated by 28 pixels and correspond to a spacing of 62 μm. This yields a spatial calibration of ~2.2(1) μm/pix for the VISAR alignment camera.

The final spatial calibration for the streak cameras is then obtained by dividing ~2.2(1) μm/pix by the corresponding magnification factor from Table IV obtained in the first calibration step. For example, the spatial calibration of VISAR 2 is found to be ~ 0.6 μm/pix. It is important to note that changing L2 modifies the spatial calibration of the VISAR alignment camera, but the magnification factors in Table IV remain constant as long as L2 is placed at the same location. The spatial calibrations for the other FoVs are then obtained by repeating the second step of the procedure for the different lenses L2.

V. EXAMPLES

A. Shock-compressed polyimide

To evaluate the quality of the spatiotemporal calibration, we measured the relation between the shock speed, U_s, and the particle velocity, U_p, for shock compressed polyimide. The results are shown in Fig. 11. The sample consisted of a 50 μm black Kapton polyimide layer from DuPont, with a 50 μm single crystal lithium fluoride (LiF) window attached at the back. DiPOLE-100X was operated with a 10 ns square pulse at three different laser energies (9.8, 18.9, and 34.4 J), corresponding to the three yellow circles in Fig. 11. The laser pulse was focused onto the sample using a 500 μm-diameter phase plate. Since the LiF window remains transparent at the measured conditions, the polyimide/LiF interface velocity was recorded using VISAR 1 and VISAR 2, equipped with 69.95 and 17.18 mm-thick fused silica etalons, respectively. These correspond to velocity-per-fringe (VPF) values of 0.7090 and 2.887 km/s at a wavelength of 532 nm. However, the presence of the LiF window introduces an

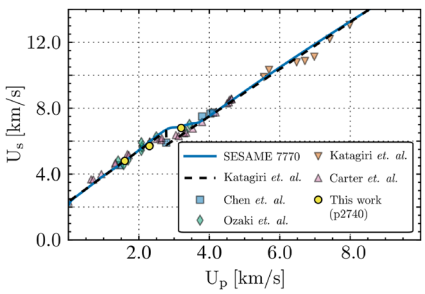


FIG. 11. Comparison of the U_s–U_p relation of shock-compressed polyimide obtained during the campaign p2740 at the HED-HIBEF instrument (yellow data points) and results from the literature. DiPOLE-100X was operated at a laser energy and DiPOLE-100X delay of 9.8 J/-15 ns, 18.9 J/-12 ns, and 34.4 J/-10 ns for each datum.

08 August 2025 08:10:42

© Author(s) 2025

optical path difference, requiring a correction to obtain the true interface velocity. This correction was applied using the calibration from Rigg *et al.*[34] The particle velocity U_p shown in Fig. 11 was determined using the impedance matching technique between the LiF window (SESAME 7271) and the polyimide sample. For polyimide, we used the U_s–U_p relation from Katagiri *et al.*[35] along with momentum conservation across the shock front to derive the P–U_p relation, with P being the sample pressure, assuming an initial density of 1.42 g/cm^3. Reshocked polyimide was modeled using the reflected Hugoniot. Shock speed U_s was obtained by measuring the breakout time of the shock at the rear surface of the polyimide as it entered the LiF window. The agreement between our measurements and previously published results demonstrates that the VISAR system at the HED-HIBEF instrument, together with the calibration procedure described in this paper, provides accurate measurements of the Hugoniot.

Finally, we compare the velocity profiles obtained from VISAR 1/2 with the results from VISAR 3, which is less prone to geometrical distortions, to assess the quality of all three VISARs calibrations. For this, we considered a 50 μm black Kapton polyimide layer from DuPont, with a 500 μm single crystal c-axis sapphire window attached at the back. We used a 10 ns, 12.4 J square pulse from DiPOLE-100X focused on the target using a 250 μm-diameter phase plate to drive a strong shock in the polyimide ablator. In Fig. 12(b), we measure the apparent velocity through the window using 31.11, 8.125, and 26.16 mm-thick etalons for VISAR 1, VISAR 2, and VISAR 3, respectively, using the Neutrino package.[36]

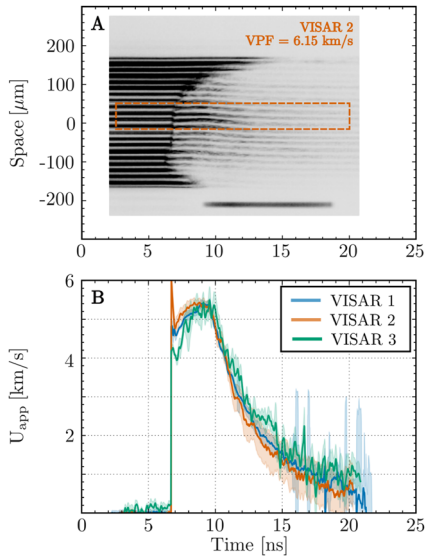


FIG. 12. Polyimide/sapphire apparent interface velocity measured using VISAR. The corrected image for VISAR 2 image is shown in (a) with the orange dashed rectangle highlighting the region of interest used for the VISAR analysis. VISAR 1 and VISAR 2 images were downsampled by a factor 2×. A median filter with a 5 super-pixel radius was applied to all VISAR images to improve the signal to noise ratio. (b) Apparent velocity history of the polyimide/sapphire interface recorded on all three VISARs.

The velocity increases from 4.7 km/s to a maximum value of 5.4 km/s, corresponding to a true velocity between 2.6 and 3.0 km/s, assuming a linear window material with a window correction given by Jensen *et al.*[37] Using the impedance matching technique between the polyimide sample (Katagiri *et al.*) and the sapphire window (SESAME 7411), we obtain a pressure between 59 and 70 GPa. This uncertainty is mainly attributed to the steadiness of the shock wave. Similar to the previous analysis, the reshocked polyimide was modeled using the reflected Hugoniot. Despite measuring at 1064 nm wavelength, the apparent velocity measured with VISAR 3 is in good agreement with the results at 532 nm wavelength and is attributed to the small variation of the sapphire window correction at the two wavelengths. Finally, we attribute the discrepancies between the extracted velocities in the vicinity of the shock breakout to differences in etalon delays for each VISAR arm.

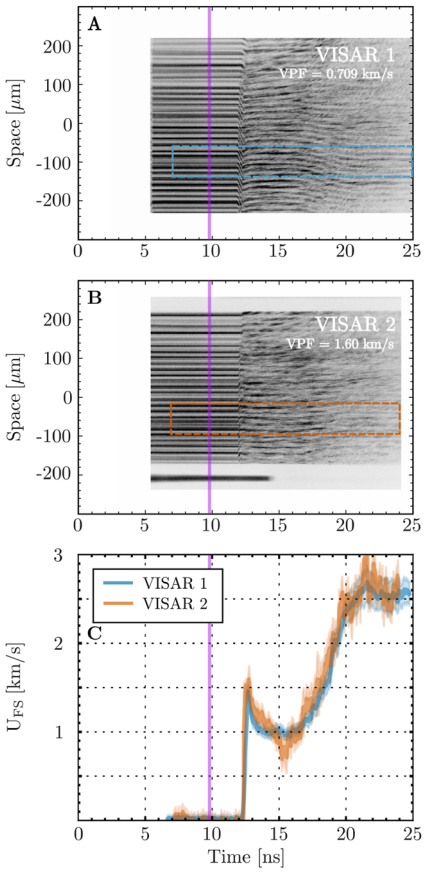


FIG. 13. Analysis of the VISAR data collected from a 100 μm-thick Si single crystal shock-compressed using a 10 ns, 29 J square pulse generated by the DiPOLE-100X laser system and focused on the target using a 500 μm diameter phase plate. The velocimetry data (c) show the free surface velocity (U_{FS}) for each VISAR (blue and orange lines) with the shaded area corresponding to the 1σ uncertainty. The corresponding corrected VISAR 2D-images are shown in (a) and (b). The vertical purple line indicates the probing time by the x-ray beam. In all images, the DiPOLE-100X laser pulse arrives at 0 ns. The dashed rectangles in (a) and (b) correspond to the region of interest used to obtain the velocity traces in (c).

08 August 2025 08:10:42

© Author(s) 2025

B. Pressure determination from shock-compressed silicon using VISAR

As a final example, we consider a 100 ± 5 μm-thick (1 0 0)-oriented silicon sample, shock-compressed using a 29 J, 10 ns square pulse generated by the DiPOLE-100X laser system. The velocity profile of the silicon–vacuum interface is recorded using VISAR 1 and VISAR 2, with 69.95 and 31.11 mm-thick fused silica etalons, respectively. These correspond to VPF constants of 0.7090 and 1.594 km/s at a wavelength of 532 nm. The 31.11 mm-thick etalon was obtained by stacking together 4.954 and 26.16 mm etalons. The corrected VISAR images, processed using the procedure described earlier, are shown in Fig. 13(a). The Si/vacuum free surface velocity, U_{FS}, was extracted using the Neutrino package.[36] The velocity profile in Fig. 13(a) shows a rapid increase as the elastic precursor, traveling at the longitudinal sound speed along the (1 0 0) crystallographic direction, reaches the rear surface of the sample in 12.4 ns. This corresponds to an elastic wave speed of 8.1 ± 0.4 km/s, in good agreement with the results of Gust and Royce.[38] Following the elastic precursor, a velocity pull-back is observed before the free surface velocity reaches a plateau at ~1 km/s, corresponding to a stress of ~9 GPa. The velocity then increases further, reaching a maximum value of 2.6 km/s, which corresponds to the inelastic wave traveling at a lower velocity than the sound speed of bulk silicon. Using the velocity–pressure relation for silicon from Smith *et al.*,[39] we estimate a particle velocity of U_P = 1.5(0.1) km/s. Applying the Hugoniot data from Paul *et al.*,[40] this corresponds to a pressure of 19(1) GPa.

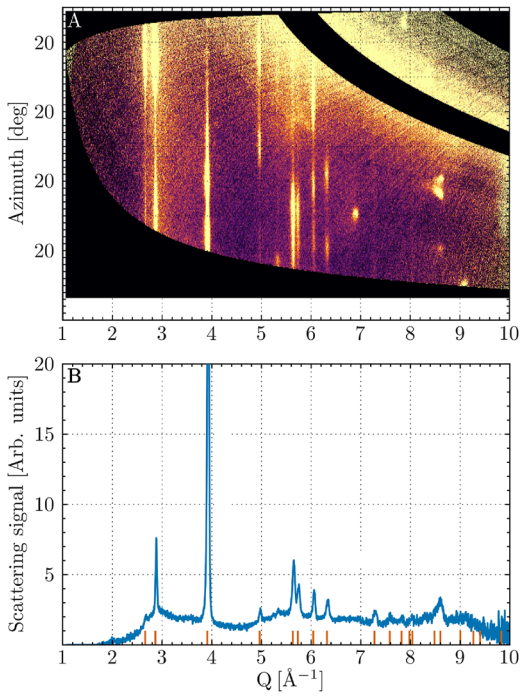


FIG. 14. 2D cake (a) and 1D integrated lineout (b) x-ray diffraction patterns measured at 18.2 keV and corresponding to the data shown in Fig. 13. The orange ticks in (b) show the positions of the high-pressure simple hexagonal phase of silicon, corresponding to a pressure of 20 GPa.

C. Pressure determination from shock-compressed silicon using X-ray diffraction

To validate the VISAR-derived pressure, we compare it with simultaneous x-ray diffraction (XRD) measurements. The European XFEL was operated at a photon energy of 18.2 keV, and the diffraction pattern was recorded in a Debye–Scherrer geometry using two Varex 4343CT flat panel detectors.[18] The long pulse laser was triggered 9.5 ns earlier than the x-ray pulse, probing prior to the breakout of the elastic precursor at the back surface. The azimuthally integrated one-dimensional diffraction pattern is shown in Fig. 14(b). We note the presence of intense diffraction spots, attributed to the uncompressed material or where the crystal has been compressed and rotated onto the Ewald sphere. We assign the observed diffraction peaks to a crystal structure of silicon with a simple hexagonal (Bravais) lattice with a c/a ratio of 0.536 and a normalized volume V/V_0 of 0.655 in the orthorhombic setting.[41,42] Using the results from McBride *et al.*,[43] we infer a pressure of 20 GPa, which is in good agreement with the pressure determined with VISAR.

VI. SUMMARY

In this paper, we describe the line-imaging VISAR system at the HED-HIBEF instrument for laser-driven compression experiments, detailing the calibration and characterization of the three arms of the two-color (532, 1064 nm) system. Each arm can be equipped with different etalons, thus enabling measurements with three different velocity sensitivities. A non-linear mapping function is applied to correct geometrical distortions in VISAR images by eliminating transverse wavevector components in the Fourier domain, effectively removing fringe curvature and space–time coupling. Using the corrected images, we establish spatial and temporal calibration parameters, facilitating the future use of the VISAR diagnostic at the HED-HIBEF instrument. The analysis of shock-compressed polyimide and silicon shows good agreement between all three VISAR arms, and the high-pressure phase crystallographic structure of a shock-compressed silicon, derived from x-ray diffraction, is consistent with the pressure determined from VISAR.

ACKNOWLEDGMENTS

We acknowledge the European XFEL in Schenefeld, Germany, for the provision of x-ray free electron laser beam time at the Scientific Instrument HED (High Energy Density Science) and would like to thank the staff for their assistance. The authors are indebted to the HIBEF user consortium for the provision of instrumentation and staff that enabled this experiment.

E.E.M. and A.D. were supported by the UK Research and Innovation Future Leaders Fellowship (Grant No. MR/W008211/1) awarded to E.E.M.

Part of this work was performed under the auspices of the U.S. Department of Energy by the Lawrence Livermore National Laboratory under Contract No. DE-AC52-07NA27344 and was supported by the Laboratory Directed Research and Development Program at LLNL (Project No. 21-ERD-032).

The DiPOLE laser system is made available to the HIBEF community on loan through a major, c. €10M joint research grant from

08 August 2025 08:10:42

© Author(s) 2025

the EPSRC (grant holder Professor Wark, Oxford) and the STFC (grant holder Professor Collier).

This work was supported by the French CNRS via AAP XFEL Instrumentation 2019, under the grant "Assessing microscopic and macroscopic electronic properties of matter under extreme conditions."

The visible-wavelength line-imaging VISAR system was provided to the HiBEF consortium by the Los Alamos National Laboratory through funding by the U.S. Department of Energy, National Nuclear Security Administration's Dynamic Materials Properties program. Part of this work was performed under the auspices of the U.S. Department of Energy through the Los Alamos National Laboratory, operated by Triad National Security, LLC, for the National Nuclear Security Administration (Contract No. 89233218CNA000001). Research presented in this paper was supported by the Department of Energy, Laboratory Directed Research and Development program at the Los Alamos National Laboratory under Project No. 20190643DR and the SLAC National Accelerator Laboratory under Contract No. DE-AC02-76SF00515.

The work at USF has been supported by Lawrence Livermore Laboratory's Academic Collaborative Team award, DOE/NNSA (Award Nos. DE-NA-0004089 and DE-NA0004234) and DOE/FES (Award No. DE-SC0024640), NSF (Award No. 2421937), and NASA (Award No. 24-XRP24_2-0176).

This work was supported by Grants Nos. EP/S022155/1 (M.I.M., M.J.D.), EP/S025065/1 (J.S.W., D.J.P., P.G.H.), and EP/S023585/1 (A.H., L.A.) from the UK Engineering and Physical Sciences Research Council.

J.S.W. and P.G.H. gratefully acknowledge support from EPSRC under research Grant No. EP/X031624.

J.D.M. is grateful to AWE for the award of CASE Studentship P030463429.

P.G.H. acknowledges support from the Oxford Centre for High Energy Density Science (OxCHEDS) under PDRA Contract No. 30469604.

D.E. and D.S.-P. from Univ. de-Valencia thank the financial support by the Spanish Ministerio de-Ciencia, Innovación y Universidades (MICIU) and the Agencia Estatal de-Investigación (MCIN/AEI/10.13039/501100011033) under Grant Nos. PID2021-125518NB-I00 and PID2022-138076NB-C41 (cofinanced by EU FEDER funds) and by the Generalitat Valenciana under Grant Nos. CIPROM/2021/075, CIAICO/2021/241, and MFA/2022/007 (funded by Next Generation EU PRTR-C17.I1).

N.J.H. and A.G. were supported by the DOE Office of Science, Fusion Energy Science, under Grant Nos. FWP 100182 and FWP 100866.

G.C. and T.-A.S. recognize support from NSF Physics Frontier Center Award No. PHY-2020249 and the U.S. Department of Energy National Nuclear Security Administration under Award No. DE-NA0003856, the University of Rochester, and the New York State Energy Research and Development Authority.

B.M. and R.S.M. acknowledge funding from the European Research Council (ERC) under the European Union's Horizon 2020 research and innovation program (Grant Agreement No. 101002868). S.M., H.G., and J.C. are funded by the European Union (ERC, HotCores, Grant No 101054994). Views and opinions expressed are however those of the author(s) only and do not necessarily reflect those of the European Union or the European Research Council. Neither the European Union nor the granting authority can be held responsible for them.

K.A., Z.K., H.P.L., R.R., and T.T. thank the DFG for support within the Research Unit FOR 2440. K.B. acknowledges financial support by the Deutsche Forschungsgemeinschaft (DFG, German Research Foundation) via project AP262/2-2 (Project No. 280637173).

Y.L. is grateful for the support from the Leader Researcher program (Grant No. NRF-2018R1A3B1052042) of the Korean Ministry of Science and ICT (MSIT).

S.P. acknowledges support from the GOtoXFEL 2023 AAP from CNRS.

AUTHOR DECLARATIONS

Conflict of Interest

The authors have no conflicts to disclose.

Author Contributions

A. Descamps: Data curation (equal); Formal analysis (equal); Investigation (equal); Methodology (equal); Software (equal); Writing – original draft (equal); Writing – review & editing (equal). **T. M. Hutchinson**: Conceptualization (equal); Validation (equal); Writing – original draft (equal); Writing – review & editing (equal). **R. Briggs**: Conceptualization (equal); Writing – review & editing (equal). **E. E. McBride**: Conceptualization (equal); Validation (equal); Writing – original draft (equal); Writing – review & editing (equal). **M. Millot**: Conceptualization (equal); Writing – review & editing (equal). **T. Michelat**: Conceptualization (equal); Software (equal); Writing – review & editing (equal). **J. H. Eggert**: Conceptualization (equal); Writing – review & editing (equal). **B. Albertazzi**: Conceptualization (equal); Writing – review & editing (equal). **L. Antonelli**: Conceptualization (equal); Writing – review & editing (equal). **M. R. Armstrong**: Conceptualization (equal); Writing – review & editing (equal). **C. Baehtz**: Conceptualization (equal); Writing – review & editing (equal). **O. B. Ball**: Conceptualization (equal); Writing – review & editing (equal). **S. Banerjee**: Conceptualization (equal); Writing – review & editing (equal). **A. B. Belonoshko**: Conceptualization (equal); Writing – review & editing (equal). **A. Benuzzi-Mounaix**: Conceptualization (equal); Writing – review & editing (equal). **C. A. Bolme**: Conceptualization (equal); Writing – review & editing (equal). **V. Bouffetier**: Conceptualization (equal); Writing – review & editing (equal). **K. Buakor**: Conceptualization (equal); Writing – review & editing (equal). **T. Butcher**: Conceptualization (equal); Writing – review & editing (equal). **V. Cerantola**: Conceptualization (equal); Writing – review & editing (equal). **J. Chantel**: Conceptualization (equal); Writing – review & editing (equal). **A. L. Coleman**: Conceptualization (equal); Writing – review & editing (equal). **J. Collier**: Conceptualization (equal); Writing – review & editing (equal). **G. Collins**: Conceptualization (equal); Writing – review & editing (equal). **A. J. Comley**: Conceptualization (equal); Writing – review & editing (equal). **F. Coppari**: Conceptualization (equal); Writing – review & editing (equal). **T. E. Cowan**: Conceptualization (equal); Writing – review & editing (equal). **C. Crépisson**: Conceptualization (equal); Writing

08 August 2025 08:10:42

© Author(s) 2025

– review & editing (equal). **G. Cristoforetti**: Conceptualization (equal); Writing – review & editing (equal). **H. Cynn**: Conceptualization (equal); Writing – review & editing (equal). **S. Di Dio Cafiso**: Conceptualization (equal); Writing – review & editing (equal). **F. Dorchies**: Conceptualization (equal); Writing – review & editing (equal). **M. J. Duff**: Conceptualization (equal); Writing – review & editing (equal). **A. Dwivedi**: Conceptualization (equal); Writing – review & editing (equal). **D. Errandonea**: Conceptualization (equal); Writing – review & editing (equal). **E. Galtier**: Conceptualization (equal); Writing – review & editing (equal). **H. Ginestet**: Conceptualization (equal); Writing – review & editing (equal). **L. Gizzi**: Conceptualization (equal); Writing – review & editing (equal). **A. Gleason**: Conceptualization (equal); Writing – review & editing (equal). **S. Goede**: Conceptualization (equal); Writing – review & editing (equal). **J. M. Gonzalez**: Conceptualization (equal); Writing – review & editing (equal). **M. G. Gorman**: Conceptualization (equal); Writing – review & editing (equal). **M. Harmand**: Conceptualization (equal); Writing – review & editing (equal). **N. J. Hartley**: Conceptualization (equal); Writing – review & editing (equal). **P. G. Heighway**: Conceptualization (equal); Writing – review & editing (equal). **C. Hernandez-Gomez**: Conceptualization (equal); Writing – review & editing (equal). **A. Higginbotham**: Conceptualization (equal); Writing – review & editing (equal). **H. Höppner**: Conceptualization (equal); Writing – review & editing (equal). **R. J. Husband**: Conceptualization (equal); Writing – review & editing (equal). **H. Hwang**: Conceptualization (equal); Writing – review & editing (equal). **J. Kim**: Conceptualization (equal); Writing – review & editing (equal). **P. Koester**: Conceptualization (equal); Writing – review & editing (equal). **Z. Konopkova**: Conceptualization (equal); Writing – review & editing (equal). **D. Kraus**: Conceptualization (equal); Writing – review & editing (equal). **A. Krygier**: Conceptualization (equal); Writing – review & editing (equal). **L. Labate**: Conceptualization (equal); Writing – review & editing (equal). **A. Laso Garcia**: Conceptualization (equal); Writing – review & editing (equal). **A. E. Lazicki**: Conceptualization (equal); Writing – review & editing (equal). **Y. Lee**: Conceptualization (equal); Writing – review & editing (equal). **P. Mason**: Conceptualization (equal); Writing – review & editing (equal). **M. Masruri**: Conceptualization (equal); Writing – review & editing (equal). **B. Massani**: Conceptualization (equal); Writing – review & editing (equal). **D. McGonegle**: Conceptualization (equal); Writing – review & editing (equal). **C. McGuire**: Conceptualization (equal); Writing – review & editing (equal). **J. D. McHardy**: Conceptualization (equal); Writing – review & editing (equal). **R. S. McWilliams**: Conceptualization (equal); Writing – review & editing (equal). **S. Merkel**: Conceptualization (equal); Writing – review & editing (equal). **G. Morard**: Conceptualization (equal); Writing – review & editing (equal). **B. Nagler**: Conceptualization (equal); Writing – review & editing (equal). **M. Nakatsutsumi**: Conceptualization (equal); Writing – review & editing (equal). **K. Nguyen-Cong**: Conceptualization (equal); Writing – review & editing (equal). **A.-M. Norton**: Conceptualization (equal); Writing – review & editing (equal). **I. I. Oleynik**: Conceptualization (equal); Writing – review & editing (equal). **C. Otzen**: Conceptualization (equal); Writing – review & editing (equal). **N. Ozaki**: Conceptualization (equal); Writing – review & editing (equal). **S. Pandolfi**: Conceptualization (equal); Writing – review & editing (equal). **D. J. Peake**: Conceptualization (equal); Writing – review & editing (equal). **A. Pelka**: Conceptualization (equal); Writing – review & editing (equal). **K. A. Pereira**: Conceptualization (equal); Writing – review & editing (equal). **J. P. Phillips**: Conceptualization (equal); Writing – review & editing (equal). **C. Prescher**: Conceptualization (equal); Writing – review & editing (equal). **T. R. Preston**: Conceptualization (equal); Writing – review & editing (equal). **L. Randolph**: Conceptualization (equal); Writing – review & editing (equal). **D. Ranjan**: Conceptualization (equal); Writing – review & editing (equal). **A. Ravasio**: Conceptualization (equal); Writing – review & editing (equal). **R. Redmer**: Conceptualization (equal); Writing – review & editing (equal). **J. Rips**: Conceptualization (equal); Writing – review & editing (equal). **D. Santamaria-Perez**: Conceptualization (equal); Writing – review & editing (equal). **D. J. Savage**: Conceptualization (equal); Writing – review & editing (equal). **M. Schoelmerich**: Conceptualization (equal); Writing – review & editing (equal). **J.-P. Schwinkendorf**: Conceptualization (equal); Writing – review & editing (equal). **S. Singh**: Conceptualization (equal); Writing – review & editing (equal). **J. Smith**: Conceptualization (equal); Writing – review & editing (equal). **R. F. Smith**: Conceptualization (equal); Writing – review & editing (equal). **A. Sollier**: Conceptualization (equal); Writing – review & editing (equal). **J. Spear**: Conceptualization (equal); Writing – review & editing (equal). **C. Spindloe**: Conceptualization (equal); Writing – review & editing (equal). **M. Stevenson**: Conceptualization (equal); Writing – review & editing (equal). **C. Strohm**: Conceptualization (equal); Writing – review & editing (equal). **T.-A. Suer**: Conceptualization (equal); Writing – review & editing (equal). **M. Tang**: Conceptualization (equal); Writing – review & editing (equal). **T. Tschentscher**: Conceptualization (equal); Writing – review & editing (equal). **M. Toncian**: Conceptualization (equal); Writing – review & editing (equal). **T. Toncian**: Conceptualization (equal); Writing – review & editing (equal). **S. J. Tracy**: Conceptualization (equal); Writing – review & editing (equal). **M. Tyldesley**: Conceptualization (equal); Writing – review & editing (equal). **C. E. Vennari**: Conceptualization (equal); Writing – review & editing (equal). **T. Vinci**: Conceptualization (equal); Writing – review & editing (equal). **T. J. Volz**: Conceptualization (equal); Writing – review & editing (equal). **J. Vorberger**: Conceptualization (equal); Writing – review & editing (equal). **J. P. S. Walsh**: Conceptualization (equal); Writing – review & editing (equal). **J. S. Wark**: Conceptualization (equal); Writing – review & editing (equal). **J. T. Willman**: Conceptualization (equal); Writing – review & editing (equal). **L. Wollenweber**: Conceptualization (equal); Writing – review & editing (equal). **U. Zastrau**: Conceptualization (equal); Writing – review & editing (equal). **E. Brambrink**: Conceptualization (lead); Investigation (lead); Methodology (lead); Supervision (lead); Writing – original draft (lead); Writing – review & editing (lead). **K. Appel**: Conceptualization (equal); Writing – review & editing (equal). **M. I. McMahon**: Conceptualization (equal); Writing – review & editing (equal).

DATA AVAILABILITY

Figures 2–4 were generated using run number 1222 in experimental campaign p2740 (https://doi.org/10.22003/XFEL.EU-DATA-002740-00).

08 August 2025 08:10:42

© Author(s) 2025

Figure 5 was generated using a reference VISAR image in run 843 in experimental campaign p2740 (https://doi.org/10.22003/XFEL.EU-DATA-002740-00).

Figures 6–8 were generated using runs 641–647 in experimental campaign p2740 (https://doi.org/10.22003/XFEL.EU-DATA-002740-00).

Figures 9 and 10 were generated using run 83 in experimental campaign p6659 (https://doi.org/10.22003/XFEL.EU-DATA-006659-00).

Figure 11 was generated using runs 157, 158, and 161 in experimental campaign p2740 (https://doi.org/10.22003/XFEL.EU-DATA-002740-00).

Figure 12 was generated using run 478 in experimental campaign p6659 (https://doi.org/10.22003/XFEL.EU-DATA-006659-00).

Figures 13 and 14 were generated using run 843 in experimental campaign p2740 (https://doi.org/10.22003/XFEL.EU-DATA-002740-00).

Table III was generated using runs 648 and 649 (for 10 ns sweep window and Sydor1/2), runs 641–647 (for 20 ns sweep window and Sydor1/2), and runs 650 and 651 (for 50 ns sweep window and Sydor1/2) in experimental campaign p2740 (https://doi.org/10.22003/XFEL.EU-DATA-002740-00). The Hamamatsu camera was calibrated using runs 73 in p900455 (10 ns sweep window), 71 in p900455 (20 ns sweep window), and 1224 in p2740 (50 ns sweep window) (https://doi.org/10.22003/XFEL.EU-DATA-900455-00).

Table IV was generated using runs 123 in p900455 for F_{L2} = 400 mm, 83 in p6659 F_{L2} = 850 mm, and 77 in p900455 for F_{L2} = 1520 mm. The cross-calibration was obtained using run 82 in p6659.

The Jupyter Notebooks used to process the VISAR images on the Maxwell cluster at the European XFEL are available at: https://github.com/adescamps59/EuXFEL-HED-VISAR.git.

REFERENCES

[1] S. H. Glenzer, B. J. MacGowan, P. Michel, N. B. Meezan, L. J. Suter, S. N. Dixit, J. L. Kline, G. A. Kyrala, D. K. Bradley, D. A. Callahan, E. L. Dewald, L. Divol, E. Dzenitis, M. J. Edwards, A. V. Hamza, C. A. Haynam, D. E. Hinkel, D. H. Kalantar, J. D. Kilkenny, O. L. Landen, J. D. Lindl, S. LePape, J. D. Moody, A. Nikroo, T. Parham, M. B. Schneider, R. P. J. Town, P. Wegner, K. Widmann, P. Whitman, B. K. F. Young, B. Van Wonterghem, L. J. Atherton, and E. I. Moses, "Symmetric inertial confinement fusion implosions at ultra-high laser energies," Science **327**, 1228–1231 (2010).

[2] R. S. Craxton, K. S. Anderson, T. R. Boehly, V. N. Goncharov, D. R. Harding, J. P. Knauer, R. L. McCrory, P. W. McKenty, D. D. Meyerhofer, J. F. Myatt, A. J. Schmitt, J. D. Sethian, R. W. Short, S. Skupsky, W. Theobald, W. L. Kruer, K. Tanaka, R. Betti, T. J. B. Collins, J. A. Delettrez, S. X. Hu, J. A. Marozas, A. V. Maximov, D. T. Michel, P. B. Radha, S. P. Regan, T. C. Sangster, W. Seka, A. A. Solodov, J. M. Soures, C. Stoeckl, and J. D. Zuegel, "Direct-drive inertial confinement fusion: A review," Phys. Plasmas **22**, 110501 (2015).

[3] A. B. Zylstra, O. A. Hurricane, D. A. Callahan, A. L. Kritcher, J. E. Ralph, H. F. Robey, J. S. Ross, C. V. Young, K. L. Baker, D. T. Casey, T. Döppner, L. Divol, M. Hohenberger, S. Le Pape, A. Pak, P. K. Patel, R. Tommasini, S. J. Ali, P. A. Amendt, L. J. Atherton, B. Bachmann, D. Bailey, L. R. Benedetti, L. Berzak Hopkins, R. Betti, S. D. Bhandarkar, J. Biener, R. M. Bionta, N. W. Birge, E. J. Bond, D. K. Bradley, T. Braun, T. M. Briggs, M. W. Bruhn, P. M. Celliers, B. Chang, T. Chapman, H. Chen, C. Choate, A. R. Christopherson, D. S. Clark, J. W. Crippen, E. L. Dewald, T. R. Dittrich, M. J. Edwards, W. A. Farmer, J. E. Field, D. Fittinghoff, J. Frenje, J. Gaffney, M. Gatu Johnson, S. H. Glenzer, G. P. Grim, S. Haan, K. D. Hahn, G. N. Hall, B. A. Hammel, J. Harte, E. Hartouni, J. E. Heebner, V. J. Hernandez, H. Herrmann, M. C. Herrmann, D. E. Hinkel, D. D. Ho, J. P. Holder, W. W. Hsing, H. Huang, K. D. Humbird, N. Izumi, L. C. Jarrott, J. Jeet, O. Jones, G. D. Kerbel, S. M. Kerr, S. F. Khan, J. Kilkenny, Y. Kim, H. Geppert Kleinrath, V. Geppert Kleinrath, C. Kong, J. M. Koning, J. J. Kroll, M. K. G. Kruse, B. Kustowski, O. L. Landen, S. Langer, D. Larson, N. C. Lemos, J. D. Lindl, T. Ma, M. J. MacDonald, B. J. MacGowan, A. J. Mackinnon, S. A. MacLaren, A. G. MacPhee, M. M. Marinak, D. A. Mariscal, E. V. Marley, L. Masse, K. Meaney, N. B. Meezan, P. A. Michel, M. Millot, J. L. Milovich, J. D. Moody, A. S. Moore, J. W. Morton, T. Murphy, K. Newman, J.-M. G. Di Nicola, A. Nikroo, R. Nora, M. V. Patel, L. J. Pelz, J. L. Peterson, Y. Ping, B. B. Pollock, M. Ratledge, N. G. Rice, H. Rinderknecht, M. Rosen, M. S. Rubery, J. D. Salmonson, J. Sater, S. Schiaffino, D. J. Schlossberg, M. B. Schneider, C. R. Schroeder, H. A. Scott, S. M. Sepke, K. Sequoia, M. W. Sherlock, S. Shin, V. A. Smalyuk, B. K. Spears, P. T. Springer, M. Stadermann, S. Stoupin, D. J. Strozzi, L. J. Suter, C. A. Thomas, R. P. J. Town, E. R. Tubman, C. Trosseille, P. L. Volegov, C. R. Weber, K. Widmann, C. Wild, C. H. Wilde, B. M. Van Wonterghem, D. T. Woods, B. N. Woodworth, M. Yamaguchi, S. T. Yang, and G. B. Zimmerman, "Burning plasma achieved in inertial fusion," Nature **601**, 542–548 (2022).

[4] H. Abu-Shawareb, R. Acree, P. Adams, J. Adams, B. Addis, R. Aden, P. Adrian, B. B. Afeyan, M. Aggleton *et al.*, "Achievement of target gain larger than unity in an inertial fusion experiment," Phys. Rev. Lett. **132**, 065102 (2024).

[5] T. Guillot, "Interiors of giant planets inside and outside the solar system," Science **286**, 72–77 (1999).

[6] A. Benuzzi-Mounaix, S. Mazevet, A. Ravasio, T. Vinci, A. Denoeud, M. Koenig, N. Amadou, E. Brambrink, F. Festa, A. Levy, M. Harmand, S. Brygoo, G. Huser, V. Recoules, J. Bouchet, G. Morard, F. Guyot, T. d. Resseguier, K. Myanishi, N. Ozaki, F. Dorchies, J. Gaudin, P. M. Leguay, O. Peyrusse, O. Henry, D. Raffestin, S. L. Pape, R. Smith, and R. Musella, "Progress in warm dense matter study with applications to planetology," Phys. Scr. **2014**(T161), 014060.

[7] F. Soubiran, B. Militzer, K. P. Driver, and S. Zhang, "Properties of hydrogen, helium, and silicon dioxide mixtures in giant planet interiors," Phys. Plasmas **24**, 041401 (2017).

[8] G. A. de Wijs, G. Kresse, L. Vočadlo, D. Dobson, D. Alfè, M. J. Gillan, and G. D. Price, "The viscosity of liquid iron at the physical conditions of the Earth's core," Nature **392**, 805–807 (1998).

[9] R. Helled, G. Mazzola, and R. Redmer, "Understanding dense hydrogen at planetary conditions," Nat. Rev. Phys. **2**, 562–574 (2020).

[10] L. B. Fletcher, H. J. Lee, T. Döppner, E. Galtier, B. Nagler, P. Heimann, C. Fortmann, S. LePape, T. Ma, M. Millot, A. Pak, D. Turnbull, D. A. Chapman, D. O. Gericke, J. Vorberger, T. White, G. Gregori, M. Wei, B. Barbrel, R. W. Falcone, C.-C. Kao, H. Nuhn, J. Welch, U. Zastrau, P. Neumayer, J. B. Hastings, and S. H. Glenzer, "Ultrabright X-ray laser scattering for dynamic warm dense matter physics," Nat. Photonics **9**, 274–279 (2015).

[11] B. J. Henderson, M. C. Marshall, T. R. Boehly, R. Paul, C. A. McCoy, S. X. Hu, D. N. Polsin, L. E. Crandall, M. F. Huff, D. A. Chin, J. J. Ruby, X. Gong, D. E. Fratanduono, J. H. Eggert, J. R. Rygg, and G. W. Collins, "Shock-compressed silicon: Hugoniot and sound speed up to 2100 GPa," Phys. Rev. B **103**, 094115 (2021).

[12] D. R. Goosman, "Analysis of the laser velocity interferometer," J. Appl. Phys. **46**, 3516–3524 (1975).

[13] L. M. Barker, M. Shahinpoor, and L. C. Chhabildas, "Experimental and diagnostic techniques," in *High-Pressure Shock Compression of Solids*, edited by J. R. Asay and M. Shahinpoor (Springer, New York, NY, 1993), pp. 43–73.

[14] P. M. Celliers, D. K. Bradley, G. W. Collins, D. G. Hicks, T. R. Boehly, and W. J. Armstrong, "Line-imaging velocimeter for shock diagnostics at the OMEGA laser facility," Rev. Sci. Instrum. **75**, 4916–4929 (2004).

[15] D. H. Dolan, "Foundations of VISAR analysis," Technical Report No. SAND2006-1950 (Sandia National Laboratories, Albuquerque, NM, 2006).

[16] P. M. Celliers and M. Millot, "Imaging velocity interferometer system for any reflector (VISAR) diagnostics for high energy density sciences," Rev. Sci. Instrum. **94**, 011101 (2023).

[17] U. Zastrau, K. Appel, C. Baehtz, O. Baehr, L. Batchelor, A. Berghäuser, M. Banjafar, E. Brambrink, V. Cerantola, T. E. Cowan, H. Damker, S. Dietrich, S. Di Dio Cafiso, J. Dreyer, H.-O. Engel, T. Feldmann, S. Findeisen, M. Foese, D. Fulla-Marsa, S. Göde, M. Hassan, J. Hauser, T. Herrmannsdörfer, H. Höppner, J. Kaa, P. Kaever, K. Knöfel, Z. Konôpková, A. Laso García, H.-P. Liermann, J. Mainberger, M. Makita, E.-C. Martens, E. E. McBride, D. Möller,

08 August 2025 08:10:42

© Author(s) 2025

M. Nakatsutsumi, A. Pelka, C. Plueckthun, C. Prescher, T. R. Preston, M. Röper, A. Schmidt, W. Seidel, J.-P. Schwinkendorf, M. O. Schoelmerich, U. Schramm, A. Schropp, C. Strohm, K. Sukharnikov, P. Talkovski, I. Thorpe, M. Toncian, T. Toncian, L. Wollenweber, S. Yamamoto, and T. Tschentscher, "The high energy density scientific instrument at the European XFEL," J. Synchrotron Radiat. **28**, 1393–1416 (2021).

[18]M. G. Gorman, D. McGonegle, R. F. Smith, S. Singh, T. Jenkins, R. S. McWilliams, B. Albertazzi, S. J. Ali, L. Antonelli, M. R. Armstrong, C. Baehtz, O. B. Ball, S. Banerjee, A. B. Belonoshko, A. Benuzzi-Mounaix, C. A. Bolme, V. Bouffetier, R. Briggs, K. Buakor, T. Butcher, S. Di Dio Cafiso, V. Cerantola, J. Chantel, A. Di Cicco, S. Clarke, A. L. Coleman, J. Collier, G. W. Collins, A. J. Comley, F. Coppari, T. E. Cowan, G. Cristoforetti, H. Cynn, A. Descamps, F. Dorchies, M. J. Duff, A. Dwivedi, C. Edwards, J. H. Eggert, D. Errandonea, G. Fiquet, E. Galtier, A. Laso Garcia, H. Ginestet, L. Gizzi, A. Gleason, S. Goede, J. M. Gonzalez, M. Harmand, N. J. Hartley, P. G. Heighway, C. Hernandez-Gomez, A. Higginbotham, H. Höppner, R. J. Husband, T. M. Hutchinson, H. Hwang, A. E. Lazicki, D. A. Keen, J. Kim, P. Koester, Z. Konopkova, D. Kraus, A. Krygier, L. Labate, Y. Lee, H.-P. Liermann, P. Mason, M. Masruri, B. Massani, E. E. McBride, C. McGuire, J. D. McHardy, S. Merkel, G. Morard, B. Nagler, M. Nakatsutsumi, K. Nguyen-Cong, A.-M. Norton, I. I. Oleynik, C. Otzen, N. Ozaki, S. Pandolfi, D. J. Peake, A. Pelka, K. A. Pereira, J. P. Phillips, C. Prescher, T. R. Preston, L. Randolph, D. Ranjan, A. Ravasio, R. Redmer, J. Rips, D. Santamaria-Perez, D. J. Savage, M. Schoelmerich, J.-P. Schwinkendorf, J. Smith, A. Sollier, J. Spear, C. Spindloe, M. Stevenson, C. Strohm, T.-A. Suer, M. Tang, M. Toncian, T. Toncian, S. J. Tracy, A. Trapananti, T. Tschentscher, M. Tyldesley, C. E. Vennari, T. Vinci, S. C. Vogel, T. J. Volz, J. Vorberger, J. P. S. Walsh, J. S. Wark, J. T. Willman, L. Wollenweber, U. Zastrau, E. Brambrink, K. Appel, and M. I. McMahon, "Shock compression experiments using the DIPOLE 100-X laser on the high energy density instrument at the European x-ray free electron laser: Quantitative structural analysis of liquid sn," J. Appl. Phys. **135**, 165902 (2024).

[19]L. M. Barker, "The development of the VISAR, and its use in shock compression science," AIP Conf. Proc. **505**, 11–18 (2000).

[20]N. H. Schiller, A. Dagen, and R. R. Alfano, "Picosecond streak cameras: Step by step calibration," Photon. Spectra **1982**(March).

[21]P. M. Celliers, G. W. Collins, L. B. Da Silva, D. M. Gold, R. Cauble, R. J. Wallace, M. E. Foord, and B. A. Hammel, "Shock-induced transformation of liquid deuterium into a metallic fluid," Phys. Rev. Lett. **84**, 5564–5567 (2000).

[22]D. G. Hicks, P. M. Celliers, G. W. Collins, J. H. Eggert, and S. J. Moon, "Shock-induced transformation of Al_2O_3 and LiF into semiconducting liquids," Phys. Rev. Lett. **91**, 035502 (2003).

[23]M. Millot, N. Dubrovinskaia, A. Černok, S. Blaha, L. Dubrovinsky, D. G. Braun, P. M. Celliers, G. W. Collins, J. H. Eggert, and R. Jeanloz, "Shock compression of stishovite and melting of silica at planetary interior conditions," Science **347**, 418–420 (2015).

[24]A. M. Manuel, M. Millot, L. G. Seppala, G. Frieders, Z. Zeid, K. Christensen, and P. M. Celliers, "Upgrades to the VISAR-streaked optical pyrometer (SOP) system on NIF," Proc. SPIE **9591**, 959104 (2015).

[25]J. E. Miller, T. R. Boehly, A. Melchior, D. D. Meyerhofer, P. M. Celliers, J. H. Eggert, D. G. Hicks, C. M. Sorce, J. A. Oertel, and P. M. Emmel, "Streaked optical pyrometer system for laser-driven shock-wave experiments on OMEGA," Rev. Sci. Instrum. **78**, 034903 (2007).

[26]M. C. Gregor, R. Boni, A. Sorce, J. Kendrick, C. A. McCoy, D. N. Polsin, T. R. Boehly, P. M. Celliers, G. W. Collins, D. E. Fratanduono, J. H. Eggert, and M. Millot, "Absolute calibration of the OMEGA streaked optical pyrometer for temperature measurements of compressed materials," Rev. Sci. Instrum. **87**, 114903 (2016).

[27]L. B. Fletcher, H. J. Lee, B. Barbrel, M. Gauthier, E. Galtier, B. Nagler, T. Döppner, S. LePape, T. Ma, A. Pak, D. Turnbull, T. White, G. Gregori, M. Wei, R. W. Falcone, P. Heimann, U. Zastrau, J. B. Hastings, and S. H. Glenzer, "Exploring Mbar shock conditions and isochorically heated aluminum at the matter in extreme conditions end station of the linac coherent light source (invited)," Rev. Sci. Instrum. **85**, 11E702 (2014).

[28]P. Datte, J. Baker, D. Bliss, N. Butler, P. Celliers, S. Cohen, M. Crosley, J. Edwards, D. Erskine, D. Fratanduono, G. Frieders, J. Galbraith, M. Hess, D. Johnson, M. Jones, K. LeChien, J. Lusk, C. Myers, T. McCarville, R. McDonald, G. Natoni, M. Olson, K. Raman, G. Robertson, R. Shelton, J. Shores, S. Speas, D. Spencer, E. V. de Dios, and N. Wong, "The design of a line velocity interferometer for any reflector for inertial confinement experiments on the Z-machine," Rev. Sci. Instrum. **91**, 043508 (2020).

[29]D. Yuan, S. Wang, H. Wei, H. Gu, Y. Dai, J. Zhong, Y. Li, G. Zhao, and J. Zhang, "Design, performance and application of a line-imaging velocity interferometer system for any reflector coupled with a streaked optical pyrometer system at the Shenguang-II upgrade laser facility," High Power Laser Sci. Eng. **12**, e6 (2024).

[30]L. M. Barker and K. W. Schuler, "Correction to the velocity-per-fringe relationship for the VISAR interferometer," J. Appl. Phys. **45**, 3692–3693 (1974).

[31]I. H. Malitson, "Interspecimen comparison of the refractive index of fused silica," J. Opt. Soc. Am. **55**, 1205–1209 (1965).

[32]P. M. Celliers, M. Millot, S. Brygoo, R. S. McWilliams, D. E. Fratanduono, J. R. Rygg, A. F. Goncharov, P. Loubeyre, J. H. Eggert, J. L. Peterson, N. B. Meezan, S. Le Pape, G. W. Collins, R. Jeanloz, and R. J. Hemley, "Insulator-metal transition in dense fluid deuterium," Science **361**, 677–682 (2018).

[33]G. R. Labaria, A. L. Warrick, P. M. Celliers, and D. H. Kalantar, "A robust in-situ warp-correction algorithm for VISAR streak camera data at the National Ignition Facility," Proc. SPIE **9345**, 93450Q (2015).

[34]P. A. Rigg, M. D. Knudson, R. J. Scharff, and R. S. Hixson, "Determining the refractive index of shocked [100] lithium fluoride to the limit of transmissibility," J. Appl. Phys. **116**, 033515 (2014).

[35]K. Katagiri, N. Ozaki, D. Murayama, K. Nonaka, Y. Hironaka, Y. Inubushi, K. Miyanishi, H. Nakamura, T. Okuchi, T. Sano, Y. Seto, K. Shigemori, K. Sueda, T. Togashi, Y. Umeda, M. Yabashi, T. Yabuuchi, and R. Kodama, "Hugoniot equation-of-state and structure of laser-shocked polyimide $C_{22}H_{10}N_2O_5$," Phys. Rev. B **105**, 054103 (2022).

[36]A. Flacco and T. Vinci, Neutrino.

[37]B. J. Jensen, D. B. Holtkamp, P. A. Rigg, and D. H. Dolan, "Accuracy limits and window corrections for photon Doppler velocimetry," J. Appl. Phys. **101**, 013523 (2007).

[38]W. H. Gust and E. B. Royce, "Axial yield strengths and two successive phase transition stresses for crystalline silicon," J. Appl. Phys. **42**, 1897–1905 (1971).

[39]R. F. Smith, C. A. Bolme, D. J. Erskine, P. M. Celliers, S. Ali, J. H. Eggert, S. L. Brygoo, B. D. Hammel, J. Wang, and G. W. Collins, "Heterogeneous flow and brittle failure in shock-compressed silicon," J. Appl. Phys. **114**, 133504 (2013).

[40]R. Paul, S. X. Hu, and V. V. Karasiev, "Anharmonic and anomalous trends in the high-pressure phase diagram of silicon," Phys. Rev. Lett. **122**, 125701 (2019).

[41]S. P. Lewis and M. L. Cohen, "Theoretical study of high-pressure orthorhombic silicon," Phys. Rev. B **48**, 16144–16147 (1993).

[42]M. I. McMahon, R. J. Nelmes, N. G. Wright, and D. R. Allan, "Pressure dependence of the *Imma* phase of silicon," Phys. Rev. B **50**, 739–743 (1994).

[43]E. E. McBride, A. Krygier, A. Ehnes, E. Galtier, M. Harmand, Z. Konôpková, H. J. Lee, H.-P. Liermann, B. Nagler, A. Pelka, M. Rödel, A. Schropp, R. F. Smith, C. Spindloe, D. Swift, F. Tavella, S. Toleikis, T. Tschentscher, J. S. Wark, and A. Higginbotham, "Phase transition lowering in dynamically compressed silicon," Nat. Phys. **15**, 89–94 (2019).

08 August 2025 08:10:42

© Author(s) 2025